

Nanoscale Heterogeneity in CsPbBr₃ and CsPbBr₃:KI Perovskite Films Revealed by Cathodoluminescence Hyperspectral Imaging

*Lethy Krishnan Jagadamma*¹⁺, *Paul R. Edwards*^{2+*}, *Robert W. Martin*², *Arvydas Ruseckas*¹,
Ifor D. W. Samuel^{1*}

Dr. L.K. Jagadamma, Dr. A. Ruseckas, Prof. I.D.W. Samuel
Organic Semiconductor Centre, SUPA, School of Physics & Astronomy, North Haugh, St
Andrews, KY16 9SS, United Kingdom

Dr. P.R. Edwards, Prof. R.W. Martin
Department of Physics, SUPA, University of Strathclyde, 107 Rottenrow, Glasgow
G4 0NG, United Kingdom

E-mail: paul.edwards@strath.ac.uk & idws@st-andrews.ac.uk

⁺ These authors contributed equally

Keywords: halide perovskites, grain-to-grain inhomogeneity, gradient in bandgap, local strain, local phase segregation

Abstract

The nanoscale morphology of solar cell materials strongly affects their performance. We report direct evidence for the existence of multiple length scales of heterogeneity in halide perovskites such as CsPbBr₃ and CsPbBr₃:KI. Contrary to the general notion of two distinct phases, our study suggests the presence of multiple phases in mixed halide perovskites. Highly spatially resolved (≈ 50 nm) cathodoluminescence maps reveal that the length scale of heterogeneity is composition dependent: smaller (≈ 200 nm) for CsPbBr₃, and larger (≈ 500 – 1000 nm) for CsPbBr₃:KI. Moreover, these nano-/micro-scale heterogeneities exist both laterally and vertically in mixed halides and correlate with high densities of carrier traps and fast trap-assisted recombination. The observed heterogeneities also lead to reduced power conversion efficiency of solar cells, higher hysteresis loss, and faster degradation. These insights argue for advanced nanoscale characterization of halide perovskites to guide reduction of heterogeneity and so improve device performance and stability.

1. Introduction

Non-radiative recombination losses in the halide perovskite solar cells reduce their efficiency below the Shockley-Queisser limit and accelerate degradation.¹⁻³ Recent studies suggest that these losses are linked to the multiple length scales of heterogeneity in the perovskite photoactive layers.⁴ These heterogeneities range across sub-grain (<100 nm), grain-to-grain (0.1–10 μm) and long-range (>10 μm) scales, arising from non-uniform chemical composition or residual strain.⁴⁻⁵ Strain accelerates the degradation of halide perovskite films by reducing the activation energy for ion migration and cause non-radiative losses.⁶⁻⁸ The polycrystalline nature and simple solution-based fabrication of halide perovskites cause localised stoichiometric deviation and extrinsic defects, such as grain boundaries.⁹ These nanoscale heterogeneities dictate the local bandgap, affect charge transport, and govern the optoelectronic properties. The distribution of non-radiative recombination across the sample surface has previously been investigated using confocal photoluminescence (PL) microscopy and very recently using photoemission electron microscopy.¹⁰⁻¹⁴ However, these measurements mostly probed the samples' near-surface region and local variations in PL *intensity* only, whereas the output performance of halide perovskite optoelectronic devices is sensitive to heterogeneity at all length scales and directions (i.e. both lateral and vertical).⁴ Vertical transport of charge carriers is central to the performance of solar cells, photodetectors and LEDs, and control of vertical heterogeneity in composition and light emission is needed to avoid unbalanced electronic transport rates, charge collection and trapping issues. Highly spatially resolved luminescence data has been reported for hybrid perovskite films using monochromatic and panchromatic cathodoluminescence (CL) mapping.¹⁵⁻¹⁹ Depth-resolved CL emission intensity maps have revealed a lateral and vertical heterogeneity in the distribution of non-radiative recombination centres. However, these reports did not reveal any heterogeneity in peak emission energy which may arise from local composition variation or local strain.

CsPbBr₃ (bandgap E_g 2.3 eV), is a promising material for LEDs,²⁰ lasers,²¹ Si/perovskite tandems,²² transparent solar cells,²³ and indoor photovoltaics,²⁴ and possesses enhanced stability to heat, oxygen and moisture compared to the hybrid CH₃NH₃PbX₃.²⁵⁻²⁸ Compared to iodides, wide bandgap lead bromide perovskites show significantly higher open circuit voltage (V_{OC}) deficits,²⁹ with > 0.7 V reported for even for the best CsPbBr₃ solar cells²⁵. Metal ion incorporation is a promising approach to enhance the stability and performance of perovskite electronic devices.³⁰⁻³³ Incorporation of potassium iodide (KI) into CH₃NH₃PbI₃ and Cs_{0.06}FA_{0.79}MA_{0.15}Pb(I_{0.85}Br_{0.15})₃ has been shown to mitigate non-radiative losses (hence improving V_{OC} and fill-factor FF) and photo-induced halide ion-migration (Br⁻).³⁴⁻³⁵ Despite these beneficial effects of KI, mixed results have been reported regarding the surface vs bulk occupancy of K⁺ and I⁻ ions, Fermi level (E_F) shifts due to doping, influence on phase segregation and composition homogeneity. Previously halide phase segregation at grain boundaries and *in situ* scanning electron CL imaging to exploit the nanoscale structural transformation in CsPbIBr₂ have been reported³⁶⁻³⁷; however the length scale of these heterogeneities, their spatial distribution and correlation with optoelectronic device performance remain open questions.

In the present study, we unravel the nanoscale heterogeneity in the material properties of CsPbBr₃ and CsPbBr₃:KI thin films and their impact on the optoelectronic device performance. Although the cathodoluminescence technique is known widely and has previously reported for halide perovskites,³⁸ our study is the first to exploit the full potential of the hyperspectral imaging mode to reveal how material properties such as bandgap, phase segregation and defects are spatially distributed with nanometer scale spatial resolution (≈ 50 nm). By combining features of both spectroscopy and microscopy, cathodoluminescence hyperspectral imaging (CLHSI) allows simultaneous collection of spatially and spectrally resolved data, with high lateral spatial resolution down to ≈ 20 nm.³⁹⁻⁴¹ We exploit the full

potential of the three-dimensional CLHSI data cube (luminescence intensity as a function of two spatial and one spectral dimension) using the spectrum-processing operations of peak fitting. By selecting suitable electron beam conditions, such nanoscale heterogeneity in light emission intensity, emission energy, and full-width at half-maximum (FWHM) is mapped for CsPbBr₃ and KI-incorporated CsPbBr₃ films. Our findings provide direct evidence for nanoscale local heterogeneity in halide perovskites, and that this correlates with the macroscopic optoelectronic properties.

2. Results and Discussion

2.1. Microstructural and optoelectronic properties

In this study we have selected low temperature (100 °C) and single step processed CsPbBr₃ and CsPbBr₃:KI films for CL hyperspectral mapping. Previous studies^{20, 42-43} have shown that CsPbBr₃ films prepared under these conditions have good light emission properties which is crucial for getting high signal-to-noise ratio CL hyperspectral mapping. Even though the wide bandgap of 2.3 eV is not ideal for outdoor solar cells applications, this bandgap is in the suitable range for indoor⁴⁴ and transparent photovoltaics⁴⁵ (~ 2 eV), and thus the obtained results are significant for various CsPbBr₃ based optoelectronic devices including photovoltaics.

Optical properties of the CsPbBr₃ and CsPbBr₃:KI films obtained using PL spectroscopy and UV-visible absorption measurements are shown in **Figure 1(a)**. The optoelectronic properties were investigated for CsBr:KI weight ratios of 1:0 and 1:0.1, as these match the previously reported KI incorporation in hybrid perovskites.³⁴ Optical properties of all the prepared films are shown in Supplementary Information (SI) (**Figure S1**). Figure 1a shows the symmetric PL emission [(Figure S1(c)] for CsPbBr₃ films at 532 nm. With KI incorporation this PL peak broadens [15 nm vs 20 nm, shown in Figure S1(b)] and redshifts to 538 nm. The UV-vis absorption spectra of the CsPbBr₃:KI films also show a redshift of ~6 nm in the absorption edge (bandgap decreasing from 2.33 to 2.30 eV). These redshifts imply that the iodide ion does not remain tightly bound to K⁺ at the surface of the perovskite but enters

the structure, affects bulk related properties, and results in the formation of a Caesium-lead mixed iodide-bromide composition. A similar effect of bandgap modification of CsPbBr₃ due to KI incorporation has been previously reported by Yousra *et al.*⁴⁶ Broader PL emission has been previously reported for mixed halides compared to pure halide perovskites.⁴⁷⁻⁴⁸

To understand how the KI incorporation influences the electronic band structure of the CsPbBr₃, the work function and valence band energy of the films were measured [**Figure 1(b) & (Figure S2)**]. The position of E_F with respect to the valence band suggests the *p*-type nature of the CsPbBr₃ films and agrees with previous reports.⁴⁹⁻⁵¹ The *p*-type conductivity is attributed to either Pb²⁺ vacancies or halide (Br⁻) interstitials.^{30, 52-53} The KI incorporation changes the electronic band structure of CsPbBr₃ with its valence band energy shifting towards the vacuum level and E_F being close to mid-gap showing the intrinsic nature of the CsPbBr₃:KI films. The slightly shallower ionization potential indicates the formation of the mixed iodide-bromide material due to the mixing of 4p⁶ and 5p⁶ orbitals from iodine and bromine atoms, respectively. This observation supports the redshift in absorption band edge and PL peak as discussed above [Figure 1(a)]. The intrinsic nature of the CsPbBr₃:KI films indicates that K⁺ ions suppress Br⁻ ion migration and interstitial halide formation as reported by Adbi-Jalebi *et al.* for KI-incorporated CH₃NH₃PbI₃ films.³⁴

The structural and morphological properties of the films were studied using X-ray diffraction (XRD) [**Figure 1(c)**] and scanning electron microscopy (SEM) measurements [**Figure 1(d)**]. The XRD pattern of CsPbBr₃ shows distinct peaks at 2θ values of 15.2°, 21.6°, 30.4°, 30.7° and 35.2° which are assigned to (010), (110), (002), (020) and (120) planes of the tetragonal phase,⁵⁵ respectively, and reveal the polycrystalline nature of the CsPbBr₃. With KI incorporation, this polycrystalline nature is preserved but the diffraction peaks broaden and the relative intensity of peaks at 21.6°, 30.4° and 35.2° is modified. This shows that KI incorporation modifies both the domain size and their preferential orientation. Previous studies

of KBr doping in CsPbBr₃ have shown increased X-ray diffraction intensity and lattice contraction due to K⁺ (1.38 Å) replacing the Cs⁺ (1.67 Å), shifting the diffraction angles to higher values.^{32-33,46} In contrast to this, our study shows that introduction of KI shifts the main X-ray diffraction peaks of CsPbBr₃ [corresponding to (010), (110) and (020) planes] towards the lower diffraction angles (15.2° vs 15.1°, 30.7° vs 30.6°, 21.6° vs 21.5°). These shifts to lower diffraction angles are an indication of preferential incorporation of the hetero-anion I⁻ (2.20 Å) replacing the Br⁻ (1.96 Å) in the CsPbBr₃ lattice and/or suppressing or compensating any effects due to K⁺ incorporation replacing the Cs⁺ (even if it occurs).

The surface morphology of the CsPbBr₃ and CsPbBr₃:KI films is further characterised using SEM images [Figure 1(d)], in which grain-like and grain-boundary-like features are visible for both films. These terms are used with caution here, as there is wide debate regarding grain and grain boundaries in the hybrid perovskites.⁵⁶⁻⁵⁷ Recently Rothmann *et al*⁵⁸ have suggested that grain boundaries can be benign by observing highly crystalline and undisturbed perovskite structure across the grain boundaries in FAPbI₃ and MAPbI₃ using atomic resolution imaging techniques. The SEM image of CsPbBr₃ shows voids with size and density of approximately 50 nm and 2 μm⁻², respectively. Incomplete surface coverage of single-step processed CsPbBr₃ has previously been reported⁴²⁻⁴³ The incorporation of KI alters the morphology, with improved surface coverage and comparable domain sizes but a different growth pattern and highly compact domains. This is in contrast to the previously reported effect of increased domain size for CsPbBr₃ grains due to KBr doping.³³ A similar increased grain size has also been reported by Nam et al for CsPbI₂Br grains due to K⁺.³² This lack of increased grain size in CsPbBr₃ due to KI incorporation again supports the inference that effective replacement of Cs⁺ ions by K⁺ in CsPbBr₃ is suppressed due to the presence of hetero-anions of I⁻. A related observation of increased surface coverage in CsPbBr₃ films with ZnO nanoparticle incorporation implies that KI modifies the nucleation properties of CsPbBr₃

films.⁴³The presence of KI in the CsPbBr₃ film is verified by Energy dispersive X-ray spectroscopy (EDS) as shown in Figure S2(c) and (d).

2.2 Depth resolved CL

In CL spectroscopy, depth resolved light emission properties of thin film samples can be obtained by varying the electron beam acceleration voltage.⁵⁹ To probe any heterogeneity in light emission across sample thickness, CL spectra were recorded for CsPbBr₃ and CsPbBr₃:KI films for electron beam voltages of 2 kV and 4 kV. Estimates of the CL generation depth under these conditions are obtained using Monte Carlo simulations⁶⁰ [**Figure 2(a)**]. For a 2 kV beam the CL emission mainly originates from the first 50 nm of material, while at 4 kV up to \approx 130 nm is probed. The corresponding depth-resolved CL spectra are shown in **Figure 2(b)**. The CL spectra from CsPbBr₃ at 2 kV and 4 kV, with the electron beam current held at \approx 1 nA, show a similar profile with peak emission at 524 nm in both cases and full widths at half maximum (FWHM) of 17 nm. The observation is different for the CsPbBr₃:KI sample, which shows a distinct *depth-dependent peak shift and peak broadening*. At 2 kV the peak is centered at 528 nm (17 nm FWHM), red shifting to 538 nm (22 nm FWHM) at 4 kV. This redshift and broadening of the CL emission with increasing depth point to vertical compositional heterogeneity for the CsPbBr₃:KI, with an iodide-rich mixed halide occupying the bulk. Any effect of beam damage is excluded here as the CL emission signal was stable over the measurement timescale (see SI for validation of this). Similarly, self-absorption can be eliminated as the cause of the redshift, as the FWHM is *broader* for the CL excited from deeper in the sample.⁶¹

Even though the smaller size of the K⁺ ions should allow them to substitute Cs⁺ ions, previous studies show that K⁺ is too small to occupy the Cs⁺ site while preserving the PbBr₆ octahedral unit.^{32, 34, 46} Moreover, Cs⁺ replacement by K⁺ would lead to lattice contraction and hence a blueshift in the bandgap. Since, in CsPbBr₃:KI, a redshift in CL emission is observed

from the bulk compared to the surface, the K^+ ions might be occupying sites near the grain boundaries. Any blueshift in bandgap due to a mixed cation $Cs_{1-x}K_x$ (even if formed in small amounts) might be dominated by the emission from the mixed bromide-iodide in the bulk.

2.3 CL hyperspectral imaging

To understand how this vertical CL heterogeneity in $CsPbBr_3:KI$ relates to the lateral heterogeneity, CL hyperspectral maps were obtained at the same two beam voltages. The 3D nature of the CLHSI data cubes makes it possible to extract the spatial distribution of spectral position, intensity, and width of one or more CL peaks in a single scan. The 2D maps in **Figure 2(c-f)** show how the emission properties of the $CsPbBr_3$ and $CsPbBr_3:KI$ thin films differ across the scanned area of $2 \times 2 \mu m$ for a 2 kV electron beam (the probed region is approximately 50 nm wide and deep, before carrier diffusion). These maps were obtained by Gaussian peak fitting to each spectrum in the hyperspectral image;⁴¹ details of this procedure is given in the SI. Corresponding SEM images are given in **Figure S3**.

Although the emission intensity [**Figure 2(c,e)**] appears more uniform for the $CsPbBr_3$ film compared to $CsPbBr_3:KI$, histogram plots of pixel frequency vs peak intensity [**Figure S4(a)**] show little difference in the intensity distributions. A comparison of the CL peak energy maps [**Figure 2(d,f)**] reveals interesting spatial distribution properties. The $CsPbBr_3$ peak energy is plotted on a 25 meV scale and is largely homogeneous with an average domain size of emission features ≈ 200 nm. However, for $CsPbBr_3:KI$, the overall emission energy is redshifted, the scale is extended to 40 meV and highly localized emissive regions with domain size $\approx 0.5 \mu m$ are observed. The overall redshift in emission energy for $CsPbBr_3:KI$ suggests the formation of mixed halides $Cs_{1-x}K_xPbBr_{3-y}I_y$ with a smaller bandgap than $CsPbBr_3$ and agrees with the UV-vis absorption and PL measurements [Figures 1(a) and 2(b)]. This redshift is seen quantitatively in histogram plots of pixel frequency vs CL peak energy [Figure S4(b)]. The small variation in emission energy (≈ 20 meV) observed for the $CsPbBr_3$ may be due to small

compositional fluctuations, strain or defects in the film.^{5, 26, 56} The larger energy variation seen in CsPbBr₃:KI can be attributed to compositional heterogeneity arising from phase segregation in mixed iodide-bromide compositions. The corresponding FWHM maps and their histograms [Figure S5(a)-(c)] show that CL emission from CsPbBr₃ is slightly broader (≈ 95 meV) compared to that from CsPbBr₃:KI (≈ 90 meV). This could be related to the differences in surface texture between the two samples.

CLHSI using a 4 kV beam increases the width and depth of the probed region to ≈ 130 nm. SEM images of the mapped area ($2 \times 2 \mu\text{m}$) are shown in Figure S6. For CsPbBr₃, the peak energy map [Figure 2(g)] shows an overall variation in peak position of ≈ 20 meV across the mapped area, similar to what observed for a 2 kV beam (probing depth ≈ 50 nm). This implies that for CsPbBr₃, the CL emission energy has no depth dependence. Also, for most grains the outer regions are found to be blue shifted compared to the grain centre as supported by the peak energy map overlaid on the SE image [Figure S7(a)]. This blueshift may be due to slight compositional variations or local compressive strain arising from the misorientation of adjacent grains during growth.^{5, 26, 56} Strain effects due to incomplete surface coverage (commonly seen in CsPbBr₃ films) also cannot be excluded.

In contrast, the peak energy map for CsPbBr₃:KI at 4 kV [Figure 2(h)] shows the CL emission to be depth dependent. Compared to the 2 kV map, [Figure 2(f)], the 4 kV map exhibits an overall redshift, larger localised emission energy domains ($\approx 0.7\text{--}1.0 \mu\text{m}$) and greater spread in peak energy (≈ 80 meV). These observations suggest that in CsPbBr₃:KI, the iodide content increases with depth, and that there is greater lateral composition heterogeneity further away from the surface region. The corresponding overlaid peak energy map and SE image are shown in Figure S6(b) and S7(b).

The CL intensity map for CsPbBr₃ [Figure 3(a)] shows intensity variations both grain-grain and within grains. In general, the darker regions correspond to areas in the proximity of

grain boundaries, as supported by the overlaid CL intensity map and topographic image [Figure 3(b)]. Local strain can also account for the less intense emission from these boundary regions.^{1, 7} Applying the peak fitting procedure to the 4kV CL hyperspectral maps from CsPbBr₃:KI reveals pixel-to-pixel variations in intensity and the appearance of multiple peaks. Since three distinct emission peaks were visible, the CL hyperspectral data set was fitted using three Gaussian functions. The peak energies were 2.32 eV, 2.24 eV and 2.15 eV and imply the existence of multiple mixed halide phases with different iodide concentrations. These different emission components were not detectable through PL or absorption measurements as presented in Figure 1(a). The intensity distribution maps for these three distinct emissions and representative fitted CL spectra are shown in Figure 3 (c–h). The main emission peak is at 2.32 eV and corresponds to the main mixed bromide-iodide related emission from CsPbBr₃:KI (matching with the PL peak shown in Figure 1(a)). The lower energy peak at 2.24 eV and 2.15 eV can be attributed to emission from increasing content of iodide rich phases. The overlay of these intensity maps with topographic images is shown in Figure 3(i–k). The corresponding SE image is shown in Figure S6(b). The 2.32 eV peak mainly comes from the grains, the maximum intensity is at the centre and reduces towards the boundaries. The 2.24 eV emission comes mostly from the grains, but small portion comes from areas between the grains. The 2.15 eV emission comes mainly from the regions between the grains and correspond to highest iodide-rich phase segregation.³⁷ The two peaks in Figure 3(h) may be due to emission from two different phases of CsPbBr_{3-x}I_x with different iodide content. To obtain the peak energy map of CsPbBr₃:KI shown in Figure 2(h) only the main CL emission at 2.32 eV is allowed to vary in full Gaussian parameter space (intensity/energy/width), while the other two (noisier) peaks are fixed in energy and width. The existence of iodide rich phases near the grain boundary region is also supported by the FWHM map analysis as described in SI [Figure S8].

This observation of multiple phases in CsPbBr₃:KI contradicts the general notion that phase segregation in mixed halides occurs as a two-phase component.⁶² Recently, Mahesh et al⁶³ predicted the possible existence of a continuum in iodide concentration or at least multiple phases in a halide segregated absorber. The consensus is that the presence of these low bandgap iodide-rich minority phases will ‘pin’ the open circuit voltage of the corresponding solar cells. Recently Nishida et al⁸ have reported that heterogeneous composition can influence the stability of the hybrid perovskites. To understand how these nanoscale heterogeneities in CsPbBr₃ and multiple phases in CsPbBr₃:KI influence the functional devices, solar cells were fabricated using these and the performance parameters and shelf life stability are explored as discussed below.

2.4 Photovoltaic and photophysical properties

Solar cells were fabricated in the *n-i-p* configuration as shown in **Figure 4(a)**, with photovoltaic performance parameters listed in **Table S1**. The current-voltage characteristics of typical devices are shown in **Figure 4(b)**. CsPbBr₃ based devices show higher power conversion efficiency (PCE) (1.16%) and lower hysteresis compared to CsPbBr₃:KI based devices (PCE 0.61%). In previous reports on CsPbBr₃ solar cells, the PCE mostly ranges from 3 to 6%⁶⁴ and the lower efficiency of our devices is due to the low processing temperature (100°C vs 300°C) and single step fabrication method used in the preparation of the active layers. These processing conditions were selected to favour high CL intensity, since CsPbBr₃ prepared under these conditions has shown to display good light emission properties.^{20, 42-43} Hence the relatively low PCE of these films does not therefore imply poor quality. The larger spatial variations in CL intensity and photon energy in CsPbBr₃:KI [**Figure 2(f,h)**] and the presence of multiple CL bands [**Figure 3(c-e)**] are indicative of energy bandgap fluctuations which can trap the photogenerated charge carriers.^{9, 65} Time-resolved photoluminescence is sensitive to the trap density in inorganic semiconductors and the PL decay measured at low excitation density is

significantly faster in CsPbBr₃:KI than CsPbBr₃ [Fig 4(c)]. This indicates faster carrier trapping in CsPbBr₃:KI and a higher density of traps. Faster PL decay in CsPbBr₃:KI also occurs on a long-time scale where trapped and un-trapped carriers are in thermal equilibrium and trap-assisted recombination dominates. This is also consistent with more trapped carriers in CsPbBr₃:KI. Unbound K⁺ ions on the perovskite surface might be contributing to this faster PL quenching in CsPbBr₃:KI. Previous studies have shown an increased lifetime of carriers in CsPbBr₃ due to KBr doping, credited to the dopant's passivation effect.^{33, 46} However, Nam *et al*³² have noted a decreased PL decay lifetime in CsPbI₂Br films doped with KI. They attribute this to the residual potassium cations failing to occupy at the A- sites of the perovskite. The PL decay in CsPbBr₃ films on a long-time scale can be fitted with a time constant $\tau_{\text{long}} \approx 12$ ns. It is interesting to note that this decay time of 12 ns is longer than the PL decay lifetime in the range 1.5 to 5 ns reported earlier for pristine CsPbBr₃ and comparable to the lifetime of ~ 12-13 ns for CsPbBr₃ films with fewer bulk defects and good exciton confinement.⁶⁶⁻⁶⁸ The longer PL decay lifetime in CsPbBr₃ films in our study indicates the high quality of the CsPbBr₃ films with less nanoscale heterogeneity and fewer bulk defects.

The faster trap-assisted recombination could be the reason for the lower J_{SC} values (Table S1) in CsPbBr₃:KI devices despite their absorption edge redshift [(Figure 1(a)]. The depth dependent compositional heterogeneity in CsPbBr₃:KI films can impede the vertical transport of the photogenerated charge carriers by adversely affecting the redistribution of the mobile ionic charge during the current-voltage scan, thus accounting for the higher hysteresis loss.⁶⁹ This vertical composition heterogeneity is detrimental to CsPbBr₃ based LEDs as well since this would result in spatial charge imbalance in electron and hole density limiting the quantum efficiency of the electroluminescence process⁷⁰. It is interesting to note that, compared to CsPbBr₃, the existence of minority phases with lower bandgap does not limit the V_{OC} from

the CsPbBr₃:KI, implying that the prevalence of these phases is below the threshold required for such losses [Table S1 and Figure 4(b)].

The shelf life stability of the CsPbBr₃ and CsPbBr₃:KI devices was tested over 20 days and is shown in Figure 4(d). For CsPbBr₃ devices, hysteresis slightly improves on ageing, whereas for CsPbBr₃:KI devices severe hysteresis loss persists. Analysis of the individual performances reveals that CsPbBr₃:KI devices suffer greater losses in V_{OC} and fill factor with ageing [Table S2-S4, and Figure S9].

For CsPbBr₃:KI films, the detailed CL hyperspectral mapping, and their optoelectronic and microstructural characterization all imply that the incorporation of a hetero-anion (of I⁻) introduced through the potassium salt, KI, is effective in tuning the composition and optical properties of CsPbBr₃. Previous studies have shown the beneficial effect of KBr doping to CsPbBr₃, through lattice contraction, suppressed recombination losses, and increased phase stability.^{32-33, 46} However, our study revealed lattice expansion, redshifted bandgap, increased recombination and higher hysteresis losses due to KI incorporation in CsPbBr₃. This implies that effect of I⁻ incorporation in replacing Br⁻ in CsPbBr₃ bulk dominates any influence due to K⁺ replacing Cs⁺.

3. Conclusion

In summary, we have revealed the presence of nanoscale heterogeneity in the material properties of the emerging optoelectronic materials of CsPbBr₃ and CsPbBr₃:KI. Our study demonstrates the existence of multiple phases with different bandgaps, with both lateral and vertical heterogeneity. The length scale of this heterogeneity is composition dependent: smaller for pure halide and larger for mixed halides. These heterogeneities in material properties cause trap-assisted recombination, adversely affecting photovoltaic devices based on CsPbBr₃:KI through lower power conversion efficiency and higher hysteresis loss. Our study further revealed that the role of K⁺ ions in replacing Cs⁺ at the A- site of the CsPbBr₃ perovskite is

suppressed in the presence of hetero-anions of I⁻, and that I⁻ preferentially replaces Br⁻ to form mixed halide perovskites. Our study strongly suggests that halide perovskite materials require detailed nanoscale characterisation of their heterogeneity, in order to guide approaches to mitigate localised stoichiometric deviations, and so realise their maximum optoelectronic functionality.

Supporting Information

Supporting information associated with this manuscript is attached as a separate file.

Competing interests:

The authors declare no competing interests

Acknowledgements

We are grateful for funding from the EPSRC under grant code EP/L017008/1. Dr. L. K. Jagadamma acknowledges support from a Marie Skłodowska-Curie Individual Fellowship (European Commission) (MCIF: No. 745776). The research data underpinning this publication can be accessed at <https://doi.org/10.17630/4b1c9e3d-7787-40c8-aade-1dcf1af62315>

References:

- (1) Luo, D.; Su, R.; Zhang, W.; Gong, Q.; Zhu, R. Minimizing non-radiative recombination losses in perovskite solar cells. *Nature Reviews Materials* **2020**, *5* (1) 44-60.
- (2) Saidaminov, M. I.; Kim, J.; Jain, A.; Quintero-Bermudez, R.; Tan, H.; Long, G.; Tan, F.; Johnston, A.; Zhao, Y.; Voznyy, O.; Sargent, E. H. Suppression of atomic vacancies via incorporation of isovalent small ions to increase the stability of halide perovskite solar cells in ambient air. *Nature Energy* **2018**, *3* (8) 648-654.
- (3) Aydin, E.; De Bastiani, M.; De Wolf, S. Defect and Contact Passivation for Perovskite Solar Cells. *Advanced Materials* **2019**, *31* (25) 1900428.
- (4) Tennyson, E. M.; Doherty, T. A. S.; Stranks, S. D. Heterogeneity at multiple length scales in halide perovskite semiconductors. *Nature Reviews Materials* **2019**, *4* (9) 573-587.
- (5) Li, X.; Luo, Y.; Holt, M. V.; Cai, Z.; Fenning, D. P. Residual Nanoscale Strain in Cesium Lead Bromide Perovskite Reduces Stability and Shifts Local Luminescence. *Chemistry of Materials* **2019**, *31* (8) 2778-2785.
- (6) Zhao, J.; Deng, Y.; Wei, H.; Zheng, X.; Yu, Z.; Shao, Y.; Shield, J. E.; Huang, J. Strained hybrid perovskite thin films and their impact on the intrinsic stability of perovskite solar cells. *Science Advances* **2017**, *3* (11) eaao5616.
- (7) Jones, T. W.; Osherov, A.; Alsari, M.; Sponseller, M.; Duck, B. C.; Jung, Y.-K.; Settens, C.; Niroui, F.; Brenes, R.; Stan, C. V.; Li, Y.; Abdi-Jalebi, M.; Tamura, N.; Macdonald, J. E.; Burghammer, M.; Friend, R. H.; Bulović, V.; Walsh, A.; Wilson, G. J.; Lilliu, S.; Stranks, S.

- D. Lattice strain causes non-radiative losses in halide perovskites. *Energy & Environmental Science* **2019**, *12* (2) 596-606.
- (8) Nishida, J.; Alfaifi, A. H.; Gray, T. P.; Shaheen, S. E.; Raschke, M. B. Heterogeneous Cation–Lattice Interaction and Dynamics in Triple-Cation Perovskites Revealed by Infrared Vibrational Nanoscopy. *ACS Energy Letters* **2020**, 1636-1643.
- (9) Jin, H.; Debroye, E.; Keshavarz, M.; Scheblykin, I. G.; Roeffaers, M. B. J.; Hofkens, J.; Steele, J. A. It's a trap! On the nature of localised states and charge trapping in lead halide perovskites. *Materials Horizons* **2020**, *7* (2) 397-410.
- (10) de Quilettes, D. W.; Vorpahl, S. M.; Stranks, S. D.; Nagaoka, H.; Eperon, G. E.; Ziffer, M. E.; Snaith, H. J.; Ginger, D. S. Impact of microstructure on local carrier lifetime in perovskite solar cells. *Science* **2015**, *348* (6235) 683-686.
- (11) de Quilettes, D. W.; Zhang, W.; Burlakov, V. M.; Graham, D. J.; Leijtens, T.; Osherov, A.; Bulović, V.; Snaith, H. J.; Ginger, D. S.; Stranks, S. D. Photo-induced halide redistribution in organic–inorganic perovskite films. *Nature Communications* **2016**, *7* (1) 11683.
- (12) de Quilettes, D. W.; Jariwala, S.; Burke, S.; Ziffer, M. E.; Wang, J. T. W.; Snaith, H. J.; Ginger, D. S. Tracking Photoexcited Carriers in Hybrid Perovskite Semiconductors: Trap-Dominated Spatial Heterogeneity and Diffusion. *ACS Nano* **2017**, *11* (11) 11488-11496.
- (13) de Quilettes, D. W.; Koch, S.; Burke, S.; Paranj, R. K.; Shropshire, A. J.; Ziffer, M. E.; Ginger, D. S. Photoluminescence Lifetimes Exceeding 8 μ s and Quantum Yields Exceeding 30% in Hybrid Perovskite Thin Films by Ligand Passivation. *ACS Energy Letters* **2016**, *1* (2) 438-444.
- (14) Doherty, T. A. S.; Winchester, A. J.; Macpherson, S.; Johnstone, D. N.; Pareek, V.; Tennyson, E. M.; Kosar, S.; Kosasih, F. U.; Anaya, M.; Abdi-Jalebi, M.; Andaji-Garmaroudi, Z.; Wong, E. L.; Madéo, J.; Chiang, Y.-H.; Park, J.-S.; Jung, Y.-K.; Petoukhoff, C. E.; Divitini, G.; Man, M. K. L.; Ducati, C.; Walsh, A.; Midgley, P. A.; Dani, K. M.; Stranks, S. D. Performance-limiting nanoscale trap clusters at grain junctions in halide perovskites. *Nature* **2020**, *580* (7803) 360-366.
- (15) Bischak, C. G.; Sanehira, E. M.; Precht, J. T.; Luther, J. M.; Ginsberg, N. S. Heterogeneous Charge Carrier Dynamics in Organic–Inorganic Hybrid Materials: Nanoscale Lateral and Depth-Dependent Variation of Recombination Rates in Methylammonium Lead Halide Perovskite Thin Films. *Nano Letters* **2015**, *15* (7) 4799-4807.
- (16) Bischak, C. G.; Hetherington, C. L.; Wu, H.; Aloni, S.; Ogletree, D. F.; Limmer, D. T.; Ginsberg, N. S. Origin of Reversible Photoinduced Phase Separation in Hybrid Perovskites. *Nano Letters* **2017**, *17* (2) 1028-1033.
- (17) Dar, M. I.; Hinderhofer, A.; Jacopin, G.; Belova, V.; Arora, N.; Zakeeruddin, S. M.; Schreiber, F.; Grätzel, M. Function Follows Form: Correlation between the Growth and Local Emission of Perovskite Structures and the Performance of Solar Cells. *Advanced Functional Materials* **2017**, *27* (26) 1701433.
- (18) Guthrey, H.; Moseley, J. A Review and Perspective on Cathodoluminescence Analysis of Halide Perovskites. *Advanced Energy Materials* **2020** 1903840.
- (19) Su, T.-S.; Eickemeyer, F. T.; Hope, M. A.; Jahanbakhshi, F.; Mladenović, M.; Li, J.; Zhou, Z.; Mishra, A.; Yum, J.-H.; Ren, D.; Krishna, A.; Ouellette, O.; Wei, T.-C.; Zhou, H.; Huang, H.-H.; Mensi, M. D.; Sivula, K.; Zakeeruddin, S. M.; Milić, J. V.; Hagfeldt, A.; Rothlisberger, U.; Emsley, L.; Zhang, H.; Grätzel, M. Crown Ether Modulation Enables over 23% Efficient Formamidinium-Based Perovskite Solar Cells. *Journal of the American Chemical Society* **2020**, *142* (47) 19980-19991.
- (20) Li, S.; Ding, H.; Cai, H.; Zhao, H.; Zhao, Y.; Yang, J.; Jin, Y.; Pan, N.; Wang, X. Realizing CsPbBr₃ Light-Emitting Diode Arrays Based on PDMS Template Confined

Solution Growth of Single-Crystalline Perovskite. *The Journal of Physical Chemistry Letters* **2020**, *11* (19) 8275-8282.

(21) Wang, X.; Chen, H.; Zhou, H.; Wang, X.; Yuan, S.; Yang, Z.; Zhu, X.; Ma, R.; Pan, A. Room-temperature high-performance CsPbBr₃ perovskite tetrahedral microlasers. *Nanoscale* **2019**, *11* (5) 2393-2400.

(22) Jaysankar, M.; Raul, B. A. L.; Bastos, J.; Burgess, C.; Weijtens, C.; Creatore, M.; Aernouts, T.; Kuang, Y. H.; Gehlhaar, R.; Hadipour, A.; Poortmans, J. Minimizing Voltage Loss in Wide-Bandgap Perovskites for Tandem Solar Cells. *Acs Energy Letters* **2019**, *4* (1) 259-264.

(23) Yuan, L.; Wang, Z.; Duan, R.; Huang, P.; Zhang, K.; Chen, Q.; Allam, N. K.; Zhou, Y.; Song, B.; Li, Y. Semi-transparent perovskite solar cells: unveiling the trade-off between transparency and efficiency. *Journal of Materials Chemistry A* **2018**, *6* (40) 19696-19702.

(24) Mathews, I.; Kantareddy, S. N. R.; Sun, S.; Layurova, M.; Thapa, J.; Correa-Baena, J.-P.; Bhattacharyya, R.; Buonassisi, T.; Sarma, S.; Peters, I. M. Self-Powered Sensors Enabled by Wide-Bandgap Perovskite Indoor Photovoltaic Cells. *Advanced Functional Materials* **2019**, *29* (42) 1904072.

(25) Li, X.; Tan, Y.; Lai, H.; Li, S.; Chen, Y.; Li, S.; Xu, P.; Yang, J. All-Inorganic CsPbBr₃ Perovskite Solar Cells with 10.45% Efficiency by Evaporation-Assisted Deposition and Setting Intermediate Energy Levels. *ACS Applied Materials & Interfaces* **2019**, *11* (33) 29746-29752.

(26) Liu, Z.; Hu, Z.; Shi, T.; Du, J.; Yang, J.; Zhang, Z.; Tang, X.; Leng, Y. Stable and enhanced frequency up-converted lasing from CsPbBr₃ quantum dots embedded in silica sphere. *Opt. Express* **2019**, *27* (7) 9459-9466.

(27) Zeng, J.; Meng, C.; Li, X.; Wu, Y.; Liu, S.; Zhou, H.; Wang, H.; Zeng, H. Interfacial-Tunneling-Effect-Enhanced CsPbBr₃ Photodetectors Featuring High Detectivity and Stability. *Advanced Functional Materials* **2019**, *29* (51) 1904461.

(28) Kulbak, M.; Gupta, S.; Kedem, N.; Levine, I.; Bendikov, T.; Hodes, G.; Cahen, D. Cesium Enhances Long-Term Stability of Lead Bromide Perovskite-Based Solar Cells. *The Journal of Physical Chemistry Letters* **2016**, *7* (1) 167-172.

(29) Zohar, A.; Kulbak, M.; Levine, I.; Hodes, G.; Kahn, A.; Cahen, D. What Limits the Open-Circuit Voltage of Bromide Perovskite-Based Solar Cells? *ACS Energy Letters* **2019**, *4* (1) 1-7.

(30) Rudd, P. N.; Huang, J. Metal Ions in Halide Perovskite Materials and Devices. *Trends in Chemistry* **2019**, *1* (4) 394-409.

(31) Abdi-Jalebi, M.; Andaji-Garmaroudi, Z.; Pearson, A. J.; Divitini, G.; Cacovich, S.; Philippe, B.; Rensmo, H.; Ducati, C.; Friend, R. H.; Stranks, S. D. Potassium- and Rubidium-Passivated Alloyed Perovskite Films: Optoelectronic Properties and Moisture Stability. *ACS Energy Letters* **2018**, *3* (11) 2671-2678.

(32) Nam, J. K.; Chai, S. U.; Cha, W.; Choi, Y. J.; Kim, W.; Jung, M. S.; Kwon, J.; Kim, D.; Park, J. H. Potassium Incorporation for Enhanced Performance and Stability of Fully Inorganic Cesium Lead Halide Perovskite Solar Cells. *Nano Letters* **2017**, *17* (3) 2028-2033.

(33) Li, Y.; Duan, J.; Yuan, H.; Zhao, Y.; He, B.; Tang, Q. Lattice Modulation of Alkali Metal Cations Doped Cs_{1-x}R_xPbBr₃ Halides for Inorganic Perovskite Solar Cells. *Solar RRL* **2018**, *2* (10) 1800164.

(34) Abdi-Jalebi, M.; Andaji-Garmaroudi, Z.; Cacovich, S.; Stavrakas, C.; Philippe, B.; Richter, J. M.; Alsari, M.; Booker, E. P.; Hutter, E. M.; Pearson, A. J.; Lilliu, S.; Savenije, T. J.; Rensmo, H.; Divitini, G.; Ducati, C.; Friend, R. H.; Stranks, S. D. Maximizing and stabilizing luminescence from halide perovskites with potassium passivation. *Nature* **2018**, *555* (7697) 497-501.

- (35) Zhao, W.; Yao, Z.; Yu, F.; Yang, D.; Liu, S. Alkali Metal Doping for Improved CH₃NH₃PbI₃ Perovskite Solar Cells. *Advanced Science* **2018**, *5* (2) 1700131.
- (36) Bischak, C. G.; Lai, M.; Fan, Z.; Lu, D.; David, P.; Dong, D.; Chen, H.; Etman, A. S.; Lei, T.; Sun, J.; Grünwald, M.; Limmer, D. T.; Yang, P.; Ginsberg, N. S. Liquid-like Interfaces Mediate Structural Phase Transitions in Lead Halide Perovskites. *Matter* **2020**, *3* (2) 534-545.
- (37) Li, W.; Rothmann, M. U.; Liu, A.; Wang, Z.; Zhang, Y.; Pascoe, A. R.; Lu, J.; Jiang, L.; Chen, Y.; Huang, F.; Peng, Y.; Bao, Q.; Etheridge, J.; Bach, U.; Cheng, Y.-B. Phase Segregation Enhanced Ion Movement in Efficient Inorganic CsPbI₂Br₂ Solar Cells. *Advanced Energy Materials* **2017**, *7* (20) 1700946.
- (38) Guthrey, H.; Moseley, J. A Review and Perspective on Cathodoluminescence Analysis of Halide Perovskites. *Advanced Energy Materials* **2020**, *10* (26) 1903840.
- (39) Martin, R. W.; Edwards, P. R.; O'Donnell, K. P.; Dawson, M. D.; Jeon, C.-W.; Liu, C.; Rice, G. R.; Watson, I. M. Cathodoluminescence spectral mapping of III-nitride structures. *physica status solidi (a)* **2004**, *201* (4) 665-672.
- (40) Edwards, P. R.; Martin, R. W. Cathodoluminescence nano-characterization of semiconductors. *Semiconductor Science and Technology* **2011**, *26* (6) 064005.
- (41) Edwards, P. R.; Jagadamma, L. K.; Bruckbauer, J.; Liu, C.; Shields, P.; Allsopp, D.; Wang, T.; Martin, R. W. High-Resolution Cathodoluminescence Hyperspectral Imaging of Nitride Nanostructures. *Microscopy and Microanalysis* **2012**, *18* (6) 1212-1219.
- (42) Li, C.; Han, C.; Zhang, Y.; Zang, Z.; Wang, M.; Tang, X.; Du, J. Enhanced photoresponse of self-powered perovskite photodetector based on ZnO nanoparticles decorated CsPbBr₃ films. *Solar Energy Materials and Solar Cells* **2017**, *172* 341-346.
- (43) Li, C.; Zang, Z.; Han, C.; Hu, Z.; Tang, X.; Du, J.; Leng, Y.; Sun, K. Highly compact CsPbBr₃ perovskite thin films decorated by ZnO nanoparticles for enhanced random lasing. *Nano Energy* **2017**, *40* 195-202.
- (44) Venkateswararao, A.; Ho, J. K. W.; So, S. K.; Liu, S.-W.; Wong, K.-T. Device characteristics and material developments of indoor photovoltaic devices. *Materials Science and Engineering: R: Reports* **2020**, *139* 100517.
- (45) Lee, K.; Um, H.-D.; Choi, D.; Park, J.; Kim, N.; Kim, H.; Seo, K. The Development of Transparent Photovoltaics. *Cell Reports Physical Science* **2020**, *1* (8) 100143.
- (46) El Ajjouri, Y.; Chirvony, V. S.; Sessolo, M.; Palazon, F.; Bolink, H. J. Incorporation of potassium halides in the mechanosynthesis of inorganic perovskites: feasibility and limitations of ion-replacement and trap passivation. *RSC Advances* **2018**, *8* (72) 41548-41551.
- (47) Pathak, S.; Sakai, N.; Wisnivesky Rocca Rivarola, F.; Stranks, S. D.; Liu, J.; Eperon, G. E.; Ducati, C.; Wojciechowski, K.; Griffiths, J. T.; Haghghirad, A. A.; Pellaroque, A.; Friend, R. H.; Snaith, H. J. Perovskite Crystals for Tunable White Light Emission. *Chemistry of Materials* **2015**, *27* (23) 8066-8075.
- (48) Brenner, P.; Glöckler, T.; Rueda-Delgado, D.; Abzieher, T.; Jakoby, M.; Richards, B. S.; Paetzold, U. W.; Howard, I. A.; Lemmer, U. Triple cation mixed-halide perovskites for tunable lasers. *Opt. Mater. Express* **2017**, *7* (11) 4082-4094.
- (49) He, Y.; Matei, L.; Jung, H. J.; McCall, K. M.; Chen, M.; Stoumpos, C. C.; Liu, Z.; Peters, J. A.; Chung, D. Y.; Wessels, B. W.; Wasielewski, M. R.; Dravid, V. P.; Burger, A.; Kanatzidis, M. G. High spectral resolution of gamma-rays at room temperature by perovskite CsPbBr₃ single crystals. *Nature Communications* **2018**, *9* (1) 1609.
- (50) Bruzzi, M.; Gabelloni, F.; Calisi, N.; Caporali, S.; Vinattieri, A. Defective States in Micro-Crystalline CsPbBr₃ and Their Role on Photoconductivity. *Nanomaterials (Basel)* **2019**, *9* (2) 177.

- (51) Zhang, H.; Liu, X.; Dong, J.; Yu, H.; Zhou, C.; Zhang, B.; Xu, Y.; Jie, W. Centimeter-Sized Inorganic Lead Halide Perovskite CsPbBr₃ Crystals Grown by an Improved Solution Method. *Crystal Growth & Design* **2017**, *17* (12) 6426-6431.
- (52) Senocrate, A.; Yang, T.-Y.; Gregori, G.; Kim, G. Y.; Grätzel, M.; Maier, J. Charge carrier chemistry in methylammonium lead iodide. *Solid State Ionics* **2018**, *321* 69-74.
- (53) He, X.; Qiu, Y.; Yang, S. Fully-Inorganic Trihalide Perovskite Nanocrystals: A New Research Frontier of Optoelectronic Materials. *Advanced Materials* **2017**, *29* (32) 1700775.
- (54) Zhou, Y.; Chen, J.; Bakr, O. M.; Sun, H.-T. Metal-Doped Lead Halide Perovskites: Synthesis, Properties, and Optoelectronic Applications. *Chemistry of Materials* **2018**, *30* (19) 6589-6613.
- (55) ICDS 109295.
- (56) Jariwala, S.; Sun, H.; Adhyaksa, G. W. P.; Lof, A.; Muscarella, L. A.; Ehrler, B.; Garnett, E. C.; Ginger, D. S. Local Crystal Misorientation Influences Non-radiative Recombination in Halide Perovskites. *Joule* **2019**, *3* (12) 3048-3060.
- (57) Liu, Y.; Collins, L.; Proksch, R.; Kim, S.; Watson, B. R.; Doughty, B.; Calhoun, T. R.; Ahmadi, M.; Ievlev, A. V.; Jesse, S.; Retterer, S. T.; Belianinov, A.; Xiao, K.; Huang, J.; Sumpter, B. G.; Kalinin, S. V.; Hu, B.; Ovchinnikova, O. S. Chemical nature of ferroelastic twin domains in CH₃NH₃PbI₃ perovskite. *Nature Materials* **2018**, *17* (11) 1013-1019.
- (58) Rothmann, M. U.; Kim, J. S.; Borchert, J.; Lohmann, K. B.; O'Leary, C. M.; Shearer, A. A.; Clark, L.; Snaith, H. J.; Johnston, M. B.; Nellist, P. D.; Herz, L. M. Atomic-scale microstructure of metal halide perovskite. *Science* **2020**, *370* (6516) eabb5940.
- (59) Petrov, V. I.; Gvozdover, R. S. Spatial resolution of cathodoluminescence scanning electron microscopy of semiconductors. *Scanning* **1991**, *13* (6) 410-414.
- (60) Drouin, D.; Couture, A. R.; Joly, D.; Tastet, X.; Aimez, V.; Gauvin, R. CASINO V2.42—A Fast and Easy-to-use Modeling Tool for Scanning Electron Microscopy and Microanalysis Users. *Scanning* **2007**, *29* (3) 92-101.
- (61) Diab, H.; Arnold, C.; Lédée, F.; Trippé-Allard, G.; Delport, G.; Vilar, C.; Bretenaker, F.; Barjon, J.; Lauret, J.-S.; Deleporte, E.; Garrot, D. Impact of Reabsorption on the Emission Spectra and Recombination Dynamics of Hybrid Perovskite Single Crystals. *The Journal of Physical Chemistry Letters* **2017**, *8* (13) 2977-2983.
- (62) Brennan, M. C.; Draguta, S.; Kamat, P. V.; Kuno, M. Light-Induced Anion Phase Segregation in Mixed Halide Perovskites. *ACS Energy Letters* **2018**, *3* (1) 204-213.
- (63) Mahesh, S.; Ball, J. M.; Oliver, R. D. J.; McMeekin, D. P.; Nayak, P. K.; Johnston, M. B.; Snaith, H. J. Revealing the origin of voltage loss in mixed-halide perovskite solar cells. *Energy & Environmental Science* **2020**, *13* (1) 258-267.
- (64) Tong, G.; Ono, L. K.; Qi, Y. Recent Progress of All-Bromide Inorganic Perovskite Solar Cells. *Energy Technology* **2020**, *8* (4) 1900961.
- (65) Unger, E. L.; Kegelmann, L.; Suchan, K.; Sörell, D.; Korte, L.; Albrecht, S. Roadmap and roadblocks for the band gap tunability of metal halide perovskites. *Journal of Materials Chemistry A* **2017**, *5* (23) 11401-11409.
- (66) Jiang, L.; Fang, Z.; Lou, H.; Lin, C.; Chen, Z.; Li, J.; He, H.; Ye, Z. Achieving long carrier lifetime and high optical gain in all-inorganic CsPbBr₃ perovskite films via top and bottom surface modification. *Physical Chemistry Chemical Physics* **2019**, *21* (39) 21996-22001.
- (67) Wang, D.; Liu, R. Q.; Tan, X.; Liu, Q.; Nan, H. R.; Sang, S. L.; Chen, F.; Huang, W. Amplified spontaneous emission properties of solution processed CsPbBr₃ perovskite thin films doped with large-group ammonium cations. *Optical Materials Express* **2020**, *10* (4) 981-997.
- (68) Wang, R.; Jia, Y.-L.; Ding, L.; He, Z.; Dong, Y.; Ma, X.-J.; Zhang, Y.; Zhou, D.-Y.; Zhu, Z.-X.; Xiong, Z.-H.; Gao, C.-H. Efficient halide perovskite light-emitting diodes with

emissive layer consisted of multilayer coatings. *Journal of Applied Physics* **2019**, *126* (16) 165502.

(69) Habisreutinger, S. N.; Noel, N. K.; Snaith, H. J. Hysteresis Index: A Figure without Merit for Quantifying Hysteresis in Perovskite Solar Cells. *ACS Energy Letters* **2018**, *3* (10) 2472-2476.

(70) Stranks, S. D.; Hoyer, R. L. Z.; Di, D.; Friend, R. H.; Deschler, F. The Physics of Light Emission in Halide Perovskite Devices. *Advanced Materials* **2019**, *31* (47) 1803336.

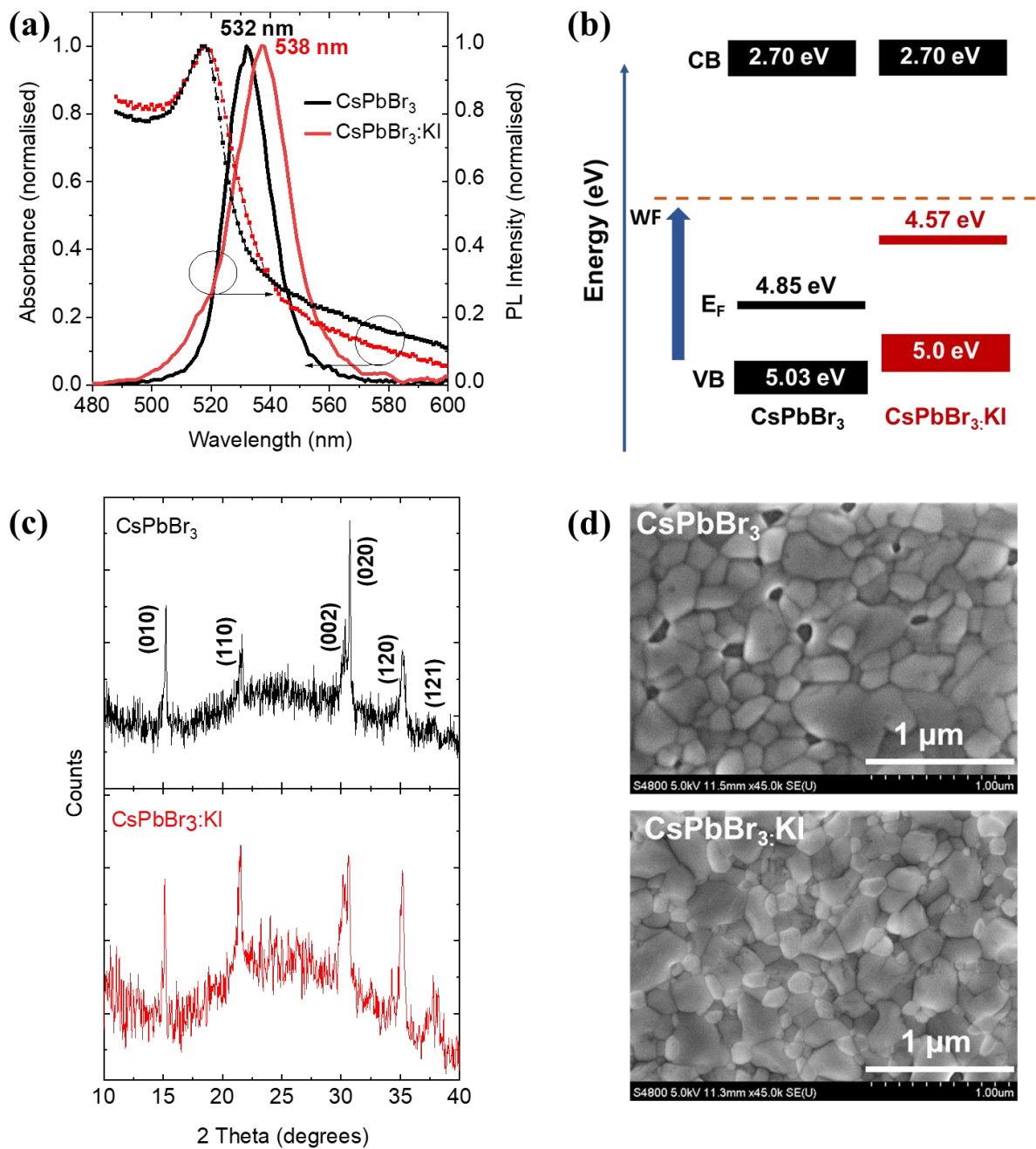


Figure 1(a) The UV-vis absorption and photoluminescence (PL) spectra of the CsPbBr₃ and CsPbBr₃:KI films. The PL excitation wavelength is 400 nm. (b) The electronic band structure of the CsPbBr₃ and CsPbBr₃:KI films obtained using Kelvin probe and ambient photoemission spectroscopy. (c) The X-ray diffraction patterns of the CsPbBr₃ and CsPbBr₃:KI films. (d) The surface morphology of the CsPbBr₃ and CsPbBr₃:KI films imaged using scanning electron microscopy. The vertical scaling has not been corrected for the 45° sample tilt. In-plane distances in the vertical dimension should be multiplied by ~1.4 to account for this

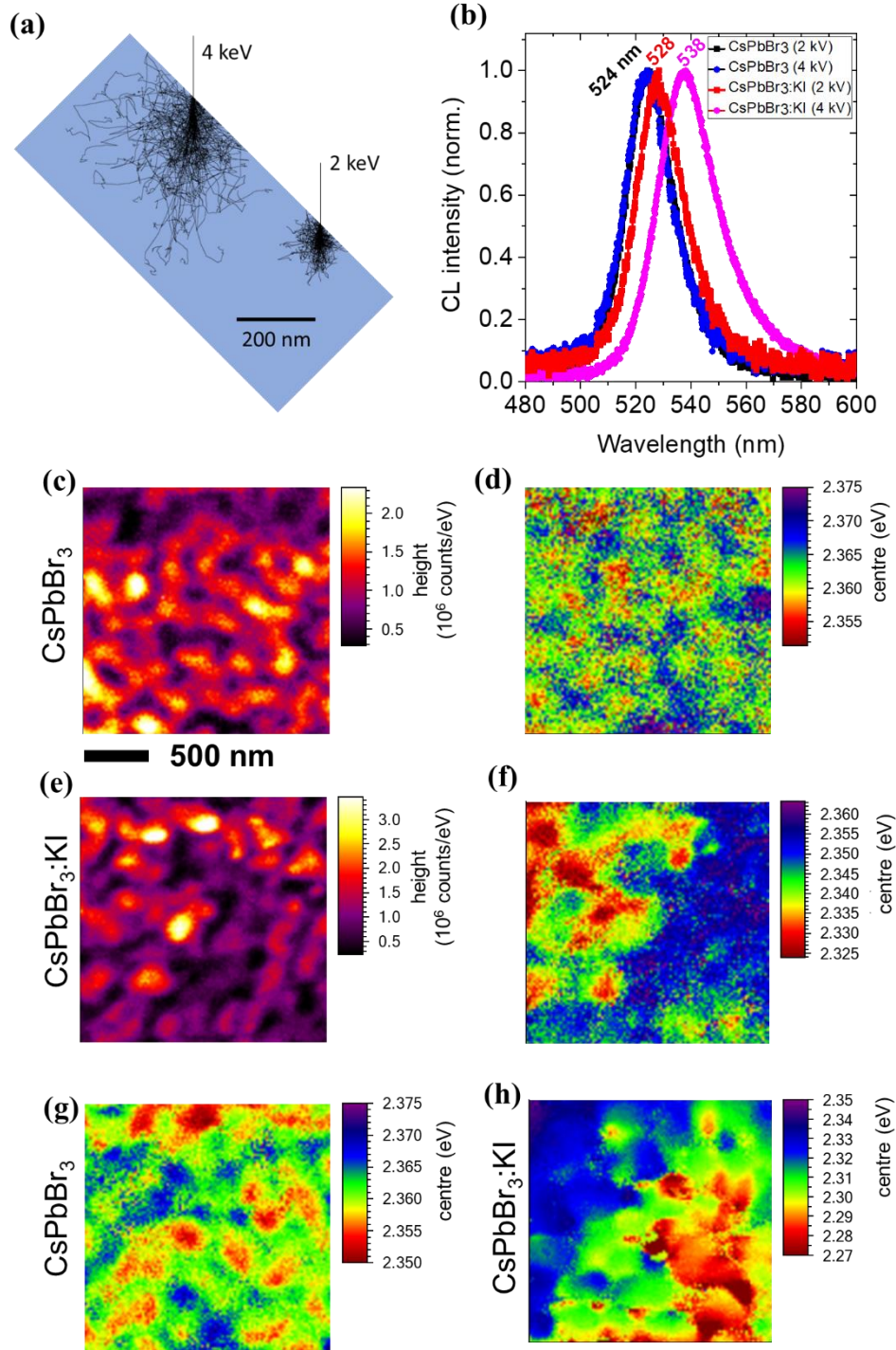


Figure 2: (a) Monte-Carlo simulation showing the electron trajectories in the CsPbBr₃ thin film sample of thickness 200 nm under electron beam acceleration voltages of 2 and 4 kV. (b) Depth resolved CL spectra from the CsPbBr₃ and CsPbBr₃:KI thin film samples. 2D spatial maps of (c) peak intensity and (d) peak emission energy of the CL emission from CsPbBr₃ at 2kV. 2D spatial maps of (e) peak intensity and (f) peak emission energy of the CL emission from CsPbBr₃:KI at 2kV. 2D spatial map of (g) peak emission energy for CsPbBr₃ at 4 kV. 2D spatial map of (h) peak emission energy for CsPbBr₃:KI at 4 kV. The vertical scaling has not been corrected for the 45° sample tilt. In-plane distances in the vertical dimension should be multiplied by ~1.4 to account for this

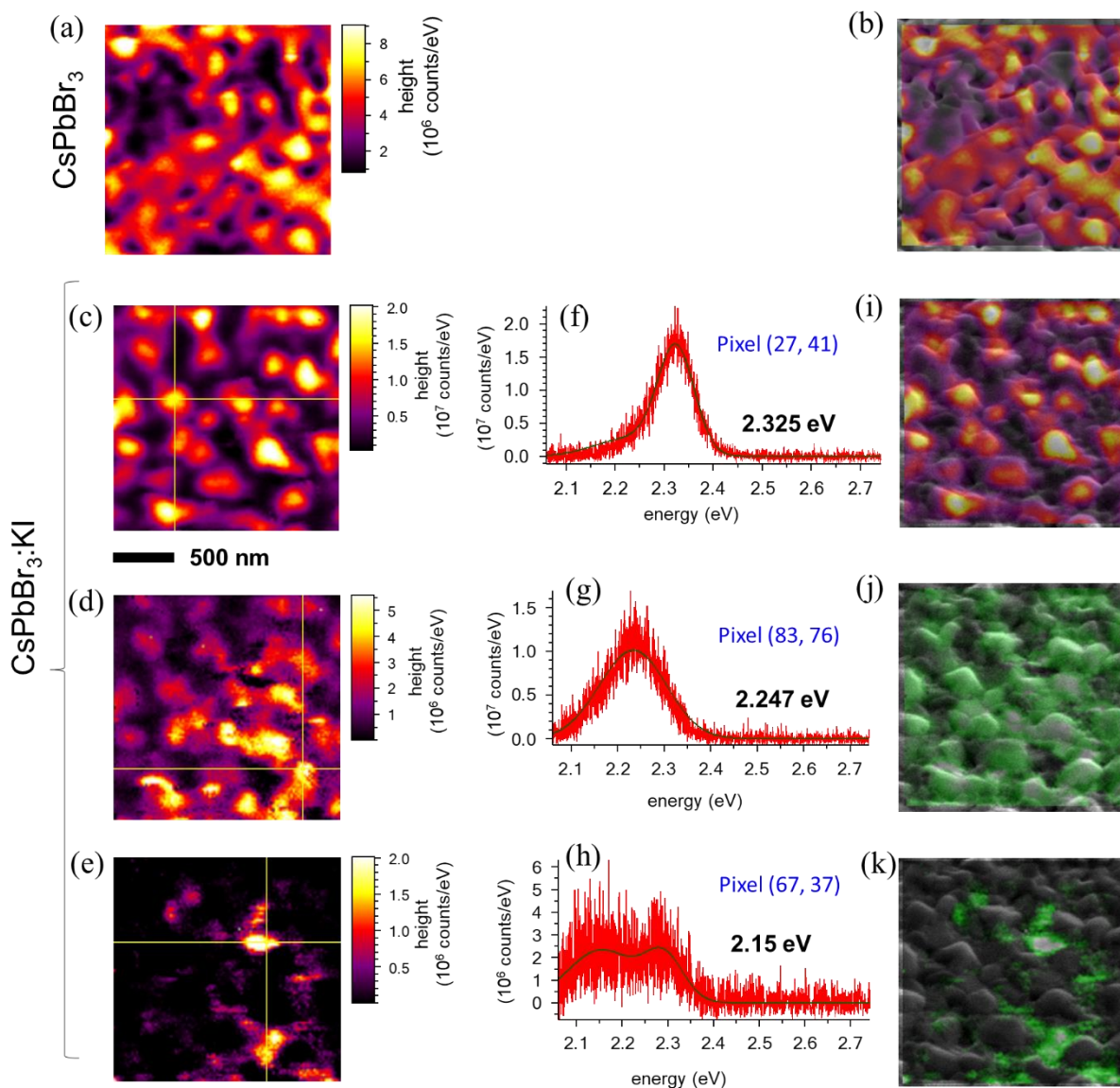


Figure 3: 2D spatial maps of (a) peak intensity of the CL emission from CsPbBr₃ obtained using a 4 kV electron beam voltage. The overlaying of the corresponding map on the secondary electron topographic image is shown in Figure 3(b). (c–e) Fitted peak intensity maps corresponding to three different components of the emission from the CsPbBr₃:KI sample under 4 kV beam excitation. The representative fitted CL emission spectra are shown in (f–h). The overlaid intensity maps on the SE images for these CL emission components are shown in (i–k). The vertical scaling has not been corrected for the 45° sample tilt. In-plane distances in the vertical dimension should be multiplied by ~1.4 to account for this. The corresponding SE image is shown in Figure S6(b).

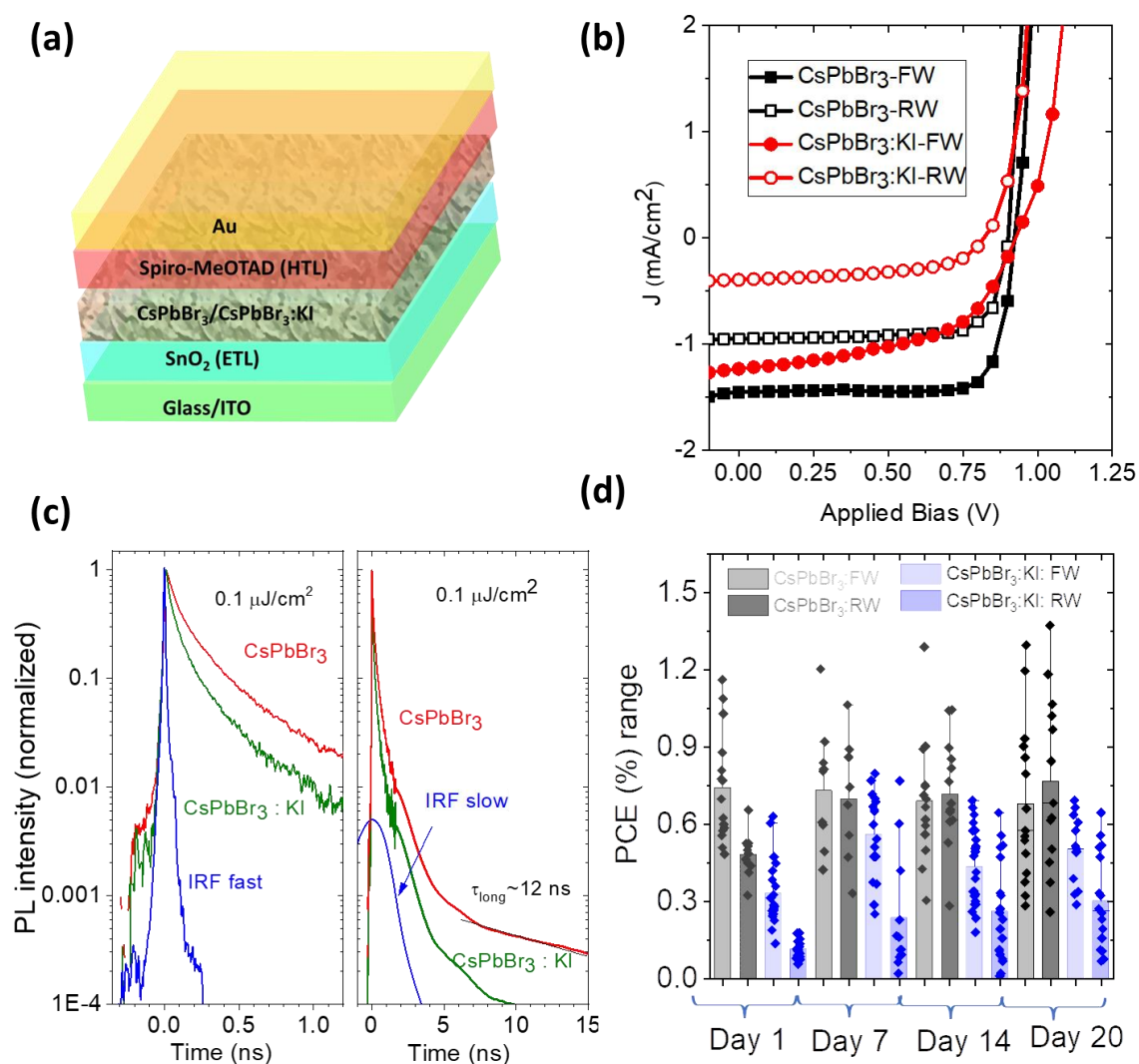
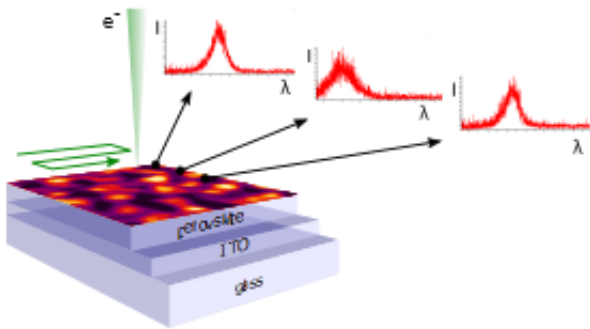


Figure 4: (a) The n-i-p device architecture used for the fabrication. (b) Current-voltage characteristics of the CsPbBr₃ and CsPbBr₃:KI based solar cells. FW stands for the forward scan and RW stands for the reverse scan. (c) Photoluminescence decays on a short (left) and long (right) time scales and the instrument response functions (IRF) of the fast and slow streak cameras. (d) Shelf-life stability study showing the variation of power conversion efficiency of the fabricated devices over a period of 20 days.

Table of Contents (TOC) graphic



Supporting Information

Nanoscale Heterogeneity in CsPbBr₃ and CsPbBr₃:KI Perovskite Films Revealed by Cathodoluminescence Hyperspectral Imaging

Lethy Krishnan Jagadamma¹⁺, Paul R. Edwards^{2+}, Robert W. Martin², Arvydas Ruseckas¹
Ifor D. W. Samuel^{1*}*

Dr. L.K. Jagadamma, Dr. A. Ruseckas, Prof. I.D.W. Samuel
Organic Semiconductor Centre, SUPA, School of Physics & Astronomy, North Haugh, St
Andrews, KY16 9SS, United Kingdom

Dr. P.R. Edwards, Prof. R.W. Martin
Department of Physics, SUPA, University of Strathclyde, 107 Rottenrow, Glasgow
G4 0NG, United Kingdom

E-mail: paul.edwards@strath.ac.uk & idws@st-andrews.ac.uk

Experimental details:

Preparation of CsPbBr₃ and CsPbBr₃:KI films:

A series of CsPbBr₃ films, approximately 200 nm thick, were prepared with different KI contents [CsBr:KI (wt% ratios) 1:0, 1:0.01, 1:0.03, 1:0.05 and 1:0.1]. To fabricate CsPbBr₃ films, the precursor solution was prepared by mixing 127.7 mg of CsBr and 146.8 mg of PbBr₂ in 1 mL of anhydrous dimethyl sulfoxide (DMSO) solvent. The mixture was then stirred at room temperature for 5–6 hours and then filtered using 0.45 μm polytetrafluoroethylene (PTFE) filters. The thin films were then obtained by spin coating at 2000 rpm for 240 seconds on cleaned ITO or glass substrates. The spin coated films were then transferred to the hotplate at 100 °C for 10 minutes. For the KI incorporation, a stock solution of 125 mg of KI was mixed with a 500 μL DMF:DMSO solvent (4:1 by volume) (DMF - dimethyl formamide). The mixture was then stirred at room temperature for ~ 3 hours and filtered using 0.45 μm PTFE filters. Then the KI solution was mixed to the CsPbBr₃ in different volume ratios of 1, 3, 5 and 10 vol%. These correspond to KI:CsBr weight ratios of 0.01, 0.03, 0.05 and 0.1 respectively. The CsPbBr₃:KI films were prepared in the same way as the CsPbBr₃ films.

Characterization of CsPbBr₃ and CsPbBr₃:KI films:

The UV-vis absorption of the prepared films was characterized using a Cary 300 spectrometer over a wavelength range of 300–800 nm. The thickness of the films was measured using Dektak II profilometer (stylus force 6 mg and a measurement range of 6.5 μm). Valence band levels of the prepared films were measured using ambient photoemission spectroscopy (KP Technology APS03 instrument). The Kelvin probe tip has a gold-alloy coating (2 mm diameter) and when used in contact potential difference (CPD) mode, vibrates at 70 Hz at an average height of 1 mm from the sample surface. For recording the ambient photoemission spectrum (APS), the sample was illuminated with a 4–5 mm diameter light spot from a tunable monochromated D₂ lamp (4–7 eV). The raw photoemission data were corrected for detector

offset, intensity normalized, then processed by a cube root power law. The energy resolution in APS mode was 50–100 meV. Steady state photoluminescence measurements were recorded at room temperature using an Edinburgh Instruments FLS980 fluorimeter using an excitation wavelength of 400 nm. The surface morphology of the prepared films was characterised using secondary electron (SE) imaging in a Hitachi S4800 scanning electron microscope (SEM). X-ray diffraction patterns of the prepared thin films were collected on a Rigaku Miniflex 600 diffractometer using Cu $K_{\alpha 1,2}$ radiation and a D/teX Ultra silicon strip detector. Data were collected in the range $5^\circ - 70^\circ 2\theta$ with a step size of 0.02° and a time per step of 0.28 s.

Cathodoluminescence hyperspectral images of the prepared films were collected using a custom-built CL set up attached to a variable pressure field emission gun SEM (FEI Quanta 250). The electron beam voltages used were 2 kV and 4 kV with a beam current of ~ 1 nA as measured using a Faraday cup. The emitted CL signal was collected using a reflecting objective with its optical axis perpendicular to the electron beam incidence direction. The angle between the surface normal and the electron beam direction is 45° . The difference in focus due to this tilt is insignificant due to the small area being mapped ($2 \times 2 \mu\text{m}$) and dynamic focus arrangement option applied. This geometry of the CL experiment has minimal influence on the spatial resolution of the obtained CL maps. CL collected through the reflecting objective was then dispersed with a 1200 lines/mm grating in a 1/8 m focal length spectrometer (Oriol MS125) and collected using a 1600-channel electron multiplying charge-coupled device (CCD, Andor Newton). The CL hyperspectral maps were collected over an area of $2 \mu\text{m} \times 2 \mu\text{m}$ using 100×100 pixels, a step size of 20 nm and 50 ms per pixel scanning time. The electron beam conditions were selected such that no beam damage is observed during the mapping and the CL signal was stable for the whole duration of the mapping experiment.

PL decays were measured in nitrogen atmosphere using a fast and slow streak camera to cover wide time range with good time resolution. The instrument response function (IFR) of the fast

camera had a full width at half maximum of 0.012 ns. Films were excited using 200 fs light pulses at 343 nm and a repetition rate of 100 kHz. The excitation spot had a Gaussian shape with an area of about 8 mm² at the e⁻² intensity of the peak. About 90% of the incident 343 nm light was absorbed in the sample. The incident pulse energy was varied with neutral density filters. About 90% of the incident light at 343 nm was absorbed in both samples. PL decays were also recorded by keeping the incident energy density to about 0.1 μJ/cm² to give an average initial excitation density of ~1×10¹⁶ cm⁻³, which is a typical carrier density in solar cells under normal operating conditions.

Fabrication and testing of the solar cells: The pre-patterned ITO-coated glass substrates were cleaned in detergent (sodium dodecyl sulphate-SDS), successively ultrasonicated in deionized water, acetone and isopropyl alcohol, and exposed to an oxygen plasma asher for 3 minutes. CsPbBr₃ and CsPbBr₃:KI films were prepared in the same manner as mentioned above. The electron transporting layer of SnO₂ film was prepared from a nanoparticle colloidal stock solution (Alfa Aesar) by diluting it in a 1:6.5 volume ratio with DI water. The mixture was then vortex mixed to ensure a uniform dispersion. The prepared solution was then spin coated onto the cleaned ITO substrates at 3000 rpm for 30 seconds and then annealed at 150°C for 30 minutes. Processing was done in air ambient conditions. The thickness of the prepared SnO₂ film was ~ 30 nm. The hole transporting layer of Spiro- MeOTAD was prepared by following the method reported in Ref: ¹ The perovskite solar cell was then completed by thermally evaporating 80 nm of Au contact. All the weighing of the perovskite materials, precursor solution preparation, stirring, perovskite active layer spin coating and the Spiro layer deposition were performed inside a nitrogen filled glove box. The current-voltage characteristics were determined under an illumination intensity of 100 mW/cm² in air using an air mass 1.5 global (AM 1.5G) Sciencetech solar simulator and a Keithley 2400 source-measure unit. The illumination intensity was verified with a calibrated monosilicon detector and a KG-5 filter.

The solar cells were applied a bias sweep of from -0.20 V to 1.5 V, with a voltage step of 10 mV and a delay time of 200 ms.

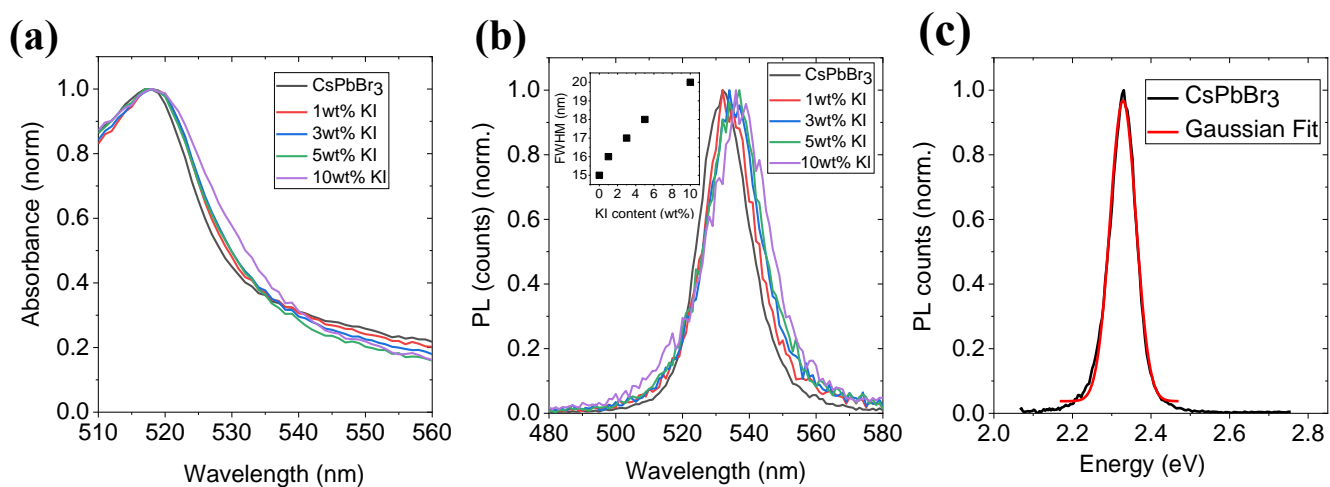


Figure S1: (a) UV-Vis absorption spectra of CsPbBr₃ and CsPbBr₃: KI films and (b) the corresponding PL emission. The inset in (b) shows how the FWHM of the PL emission spectra varies with KI content. The symmetric nature of the CsPbBr₃ PL emission is shown in Figure (c).

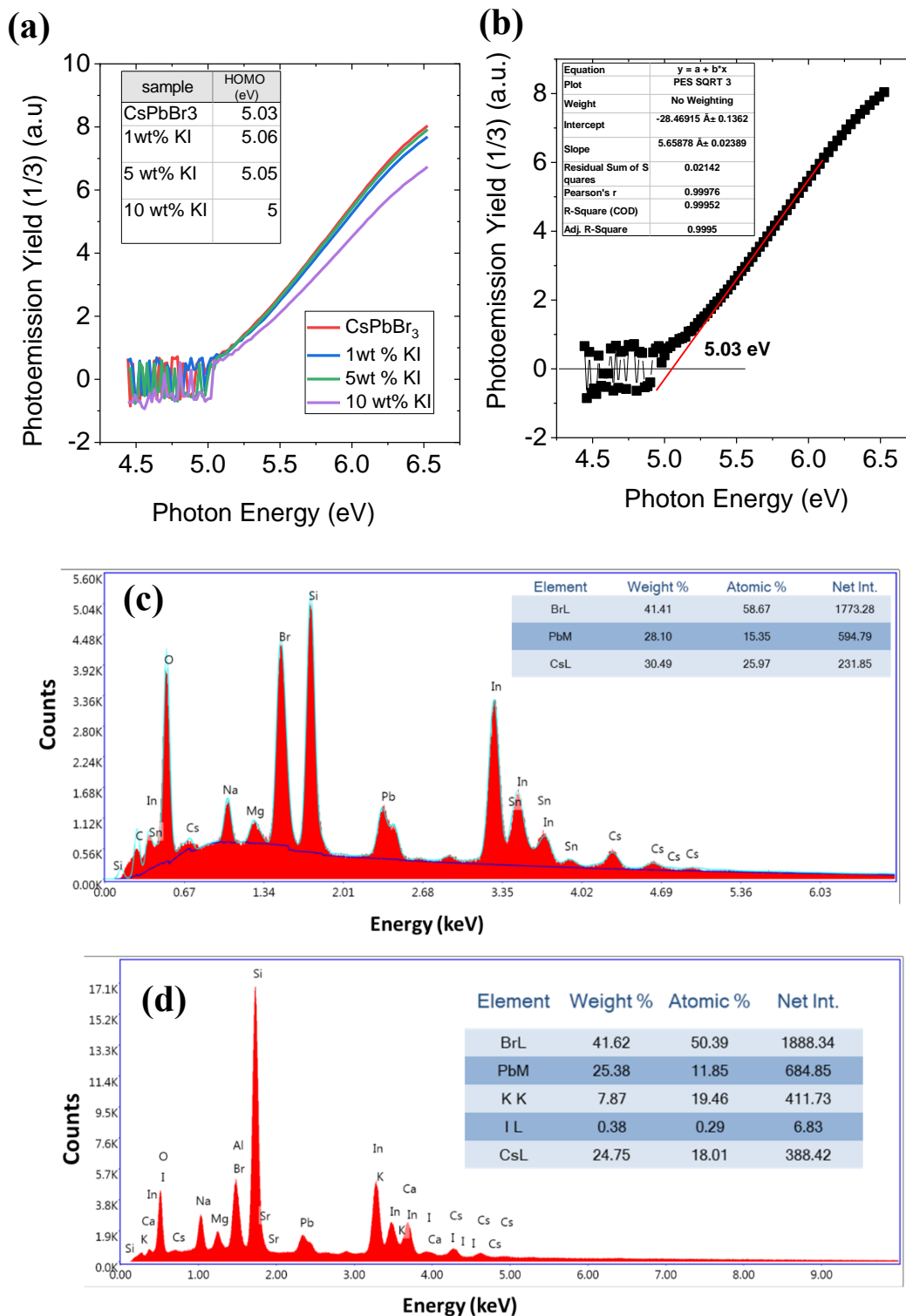


Figure S2: (a) Ambient photoemission spectra (APS) of CsPbBr₃ and CsPbBr₃:KI films. (b) Typical example showing the fitting of the APS spectra to obtain the HOMO values. (c) EDS spectrum for CsPbBr₃ and (d) EDS spectrum for CsPbBr₃:KI.

In the EDS spectra, the peaks corresponding to In and O are from the ITO substrate and the peaks from Si, Mg and Na are from the glass substrate. These extra elements have been excluded from the analysis and the results are normalized to 100%. The elemental analysis in the inset of Figure S2(d) shows the presence of K and I for CsPbBr₃:KI sample

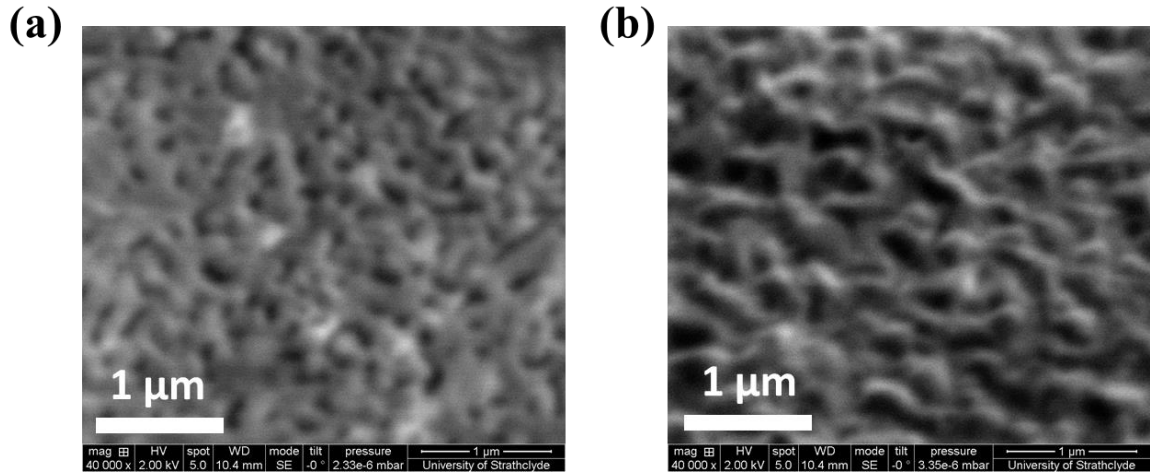


Figure S3: Scanning electron microscopy images of (a) CsPbBr₃ and (b) CsPbBr₃:KI thin films obtained using a 2 kV electron beam voltage. The low resolution of these SEM images is due to the low beam voltage (to obtain the near-surface CL properties) and the high current (~ 1 nA) set for the CL measurement. The vertical scaling has not been corrected for the 45° sample tilt. In-plane distances in the vertical dimension should be multiplied by ~1.4 to account for this

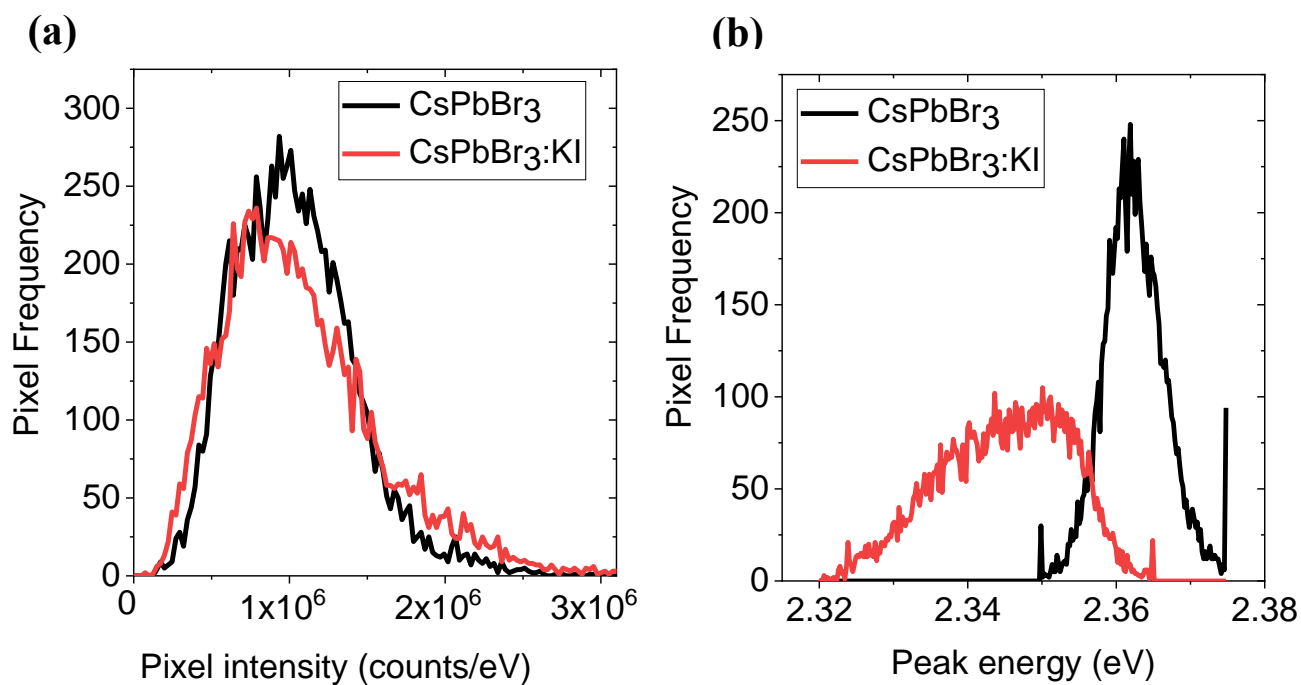


Figure S4: Histograms comparing distributions of (a) CL peak intensity and (b) CL peak energy for the two samples measured at 2 kV. These correspond to the images shown in Fig 2(c & e) and 2(d & f) respectively.

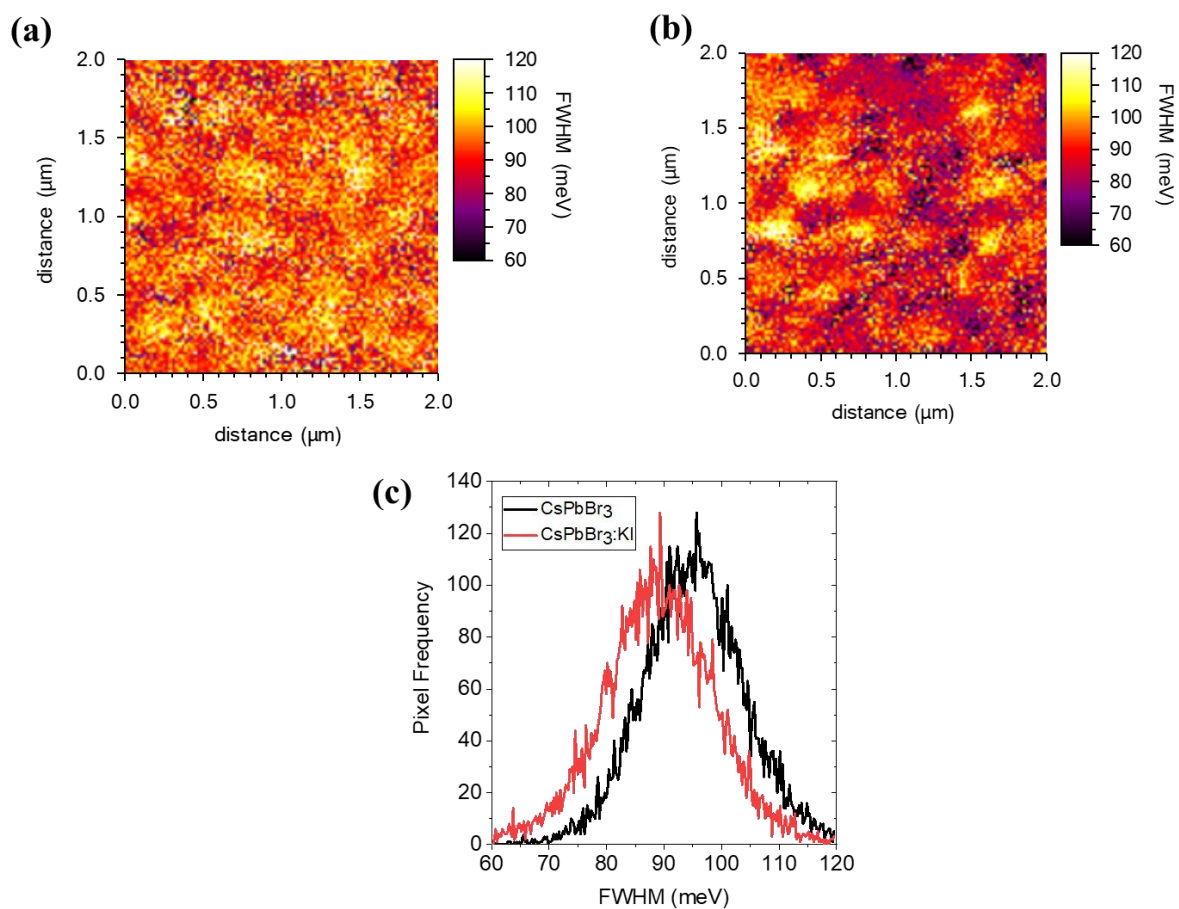


Figure S5: 2D spatial maps of FWHM of the CL emission from (a) CsPbBr₃ and (b) CsPbBr₃:KI thin films obtained using a 2 kV electron beam voltage. The vertical scaling has not been corrected for the 45° sample tilt. In-plane distances in the vertical dimension should be multiplied by ~1.4 to account for this. (c) Histograms comparing distributions of CL peak FWHM for the two samples measured at 2 kV. These correspond to the images shown in Fig (a & b).

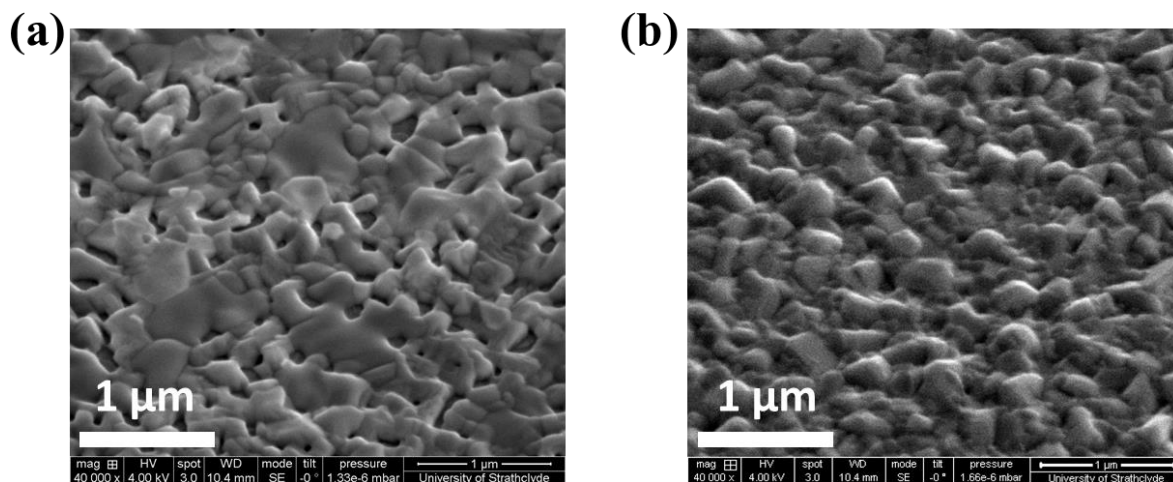


Figure S6: Scanning electron microscopy images of (a) CsPbBr₃ and (b) CsPbBr₃:KI thin films obtained using a 4 kV electron beam voltage. The vertical scaling has not been corrected for the 45° sample tilt. In-plane distances in the vertical dimension should be multiplied by ~1.4 to account for this.

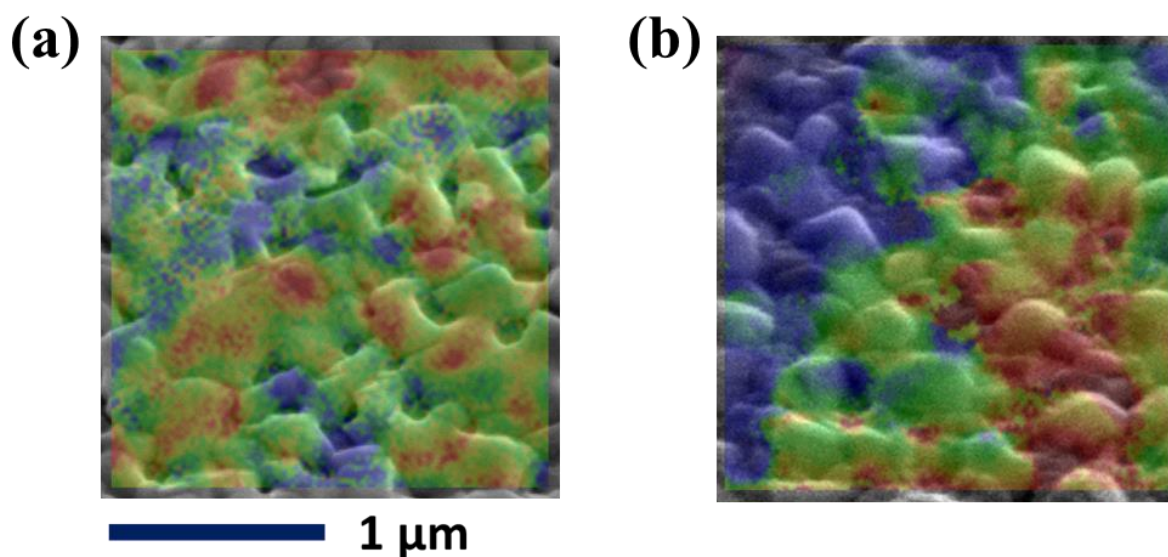


Figure S7: (a) The overlaying of the 2D spatial maps of CL peak emission energy from CsPbBr₃ obtained using a 4 kV electron beam voltage with the corresponding secondary electron topographic image. (b) The overlaying of the 2D spatial maps of CL peak emission energy from CsPbBr₃:KI obtained using a 4 kV electron beam voltage with the corresponding secondary electron topographic image. This overlaying allows the inhomogeneity in light emission to be correlated with the position of the grain-like and grain boundary-like regions. The secondary electron images are shown in Figure S6(a) and (b).

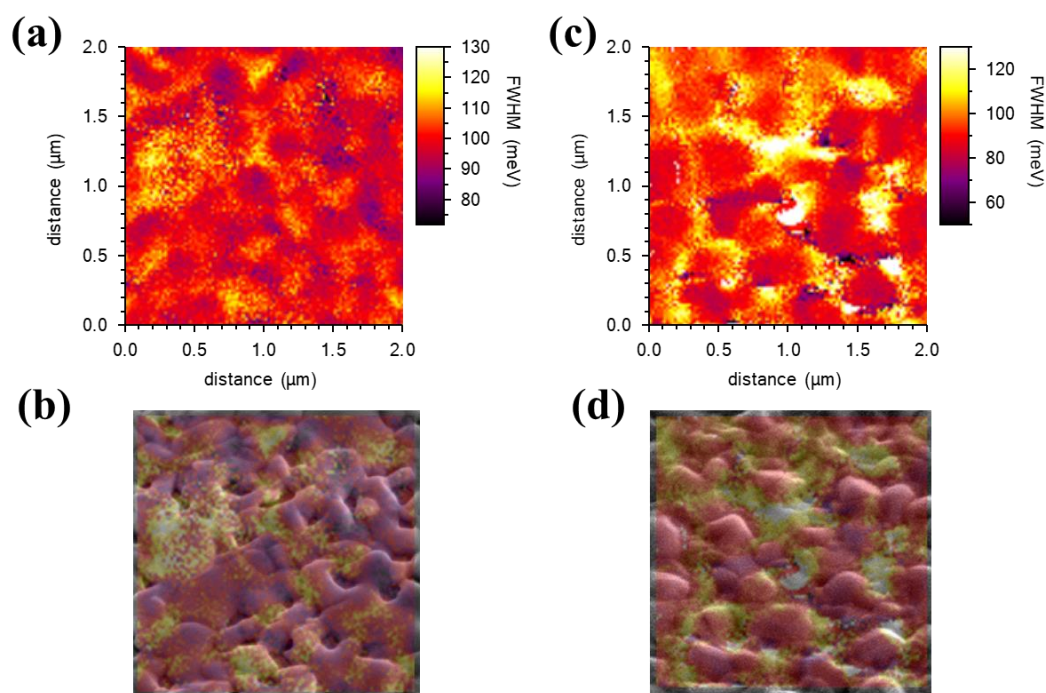


Figure S8: 2D spatial maps of (a) FWHM of the CL emission from CsPbBr₃ obtained using a 4 kV electron beam voltage. The overlaying of the corresponding map on the secondary electron topographic image is shown in Figure (b). 2D spatial maps of (c) FWHM of the CL emission from CsPbBr₃:KI obtained using a 4 kV electron beam voltage. The overlaying of the corresponding map on the secondary electron topographic image is shown in Figure (d). The secondary electron images are shown in Figure S6(a) and (b).

The FWHM map for CsPbBr₃ [Figure S9(a)] shows distributions corresponding to 90–110 meV and no significant variation across the grains or near the grain boundary regions. In the case of CsPbBr₃:KI, the overlaying of the FWHM map [Figure S9(c) & (d)] with the topographic image shows that the emission with broader FWHM is associated mainly with grain boundary regions. The FWHM of CL emission from the grains is ≈ 90 meV whereas from the grain boundary regions it is ≈ 110 meV. This approximately 20 meV broader CL emission from the grain boundary regions supports the inference from Figure 3 that the mixed iodide-bromide phases with higher iodide content mainly decorate the grain boundaries.

Table S1: Photovoltaic performance parameters of the CsPbBr₃ and CsPbBr₃:KI based devices (Day 1). The performance parameters are averaged over 12-18 devices. The \pm sign shows the standard deviation of the performance parameters.

Active layer'	FW/RW	J _{sc} (mA/cm ²)	V _{oc} (V)	FF (%)	PCE Avg (%)	PCE best (%)
CsPbBr ₃	FW	1.14±0.27	0.918±0.130	71.8±9.07	0.74±0.21	1.16
	RW	0.91±0.25	0.915±0.079	61.3±14.3	0.48±0.08	0.66
CsPbBr ₃ :KI	FW	0.52±0.23	0.961±0.083	67.5±8.4	0.33±0.13	0.61
	RW	0.27±0.06	0.859±0.143	50.4±10.7	0.12±0.04	0.18

Table S2: Photovoltaic performance parameters of the CsPbBr₃ and CsPbBr₃:KI based devices (Day 7). The performance parameters are averaged over 12–18 devices. The ± sign shows the standard deviation of the performance parameters.

Active layer	FW/RW	J _{sc} (mA/cm ²)	V _{oc} (V)	FF (%)	PCE Avg (%)	PCE best (%)
CsPbBr ₃	FW	1.16±0.20	1.03±0.09	60.7±12.2	0.73±0.23	1.2
	RW	1.11±0.19	1.08±0.11	56.7±7.9	0.70±0.24	1.06
CsPbBr ₃ :KI	FW	0.95±0.33	0.987±0.034	61.9±12.7	0.56±0.17	0.79
	RW	0.80±0.34	0.707±0.326	38.2±17.7	0.24±0.25	0.77

Table S3: Photovoltaic performance parameters of the CsPbBr₃ and CsPbBr₃:KI based devices (Day 14). The performance parameters are averaged over 12–18 devices. The ± sign shows the standard deviation of the performance parameters.

Active layer	FW/RW	J _{sc} (mA/cm ²)	V _{oc} (V)	FF (%)	PCE Avg (%)	PCE best (%)
CsPbBr ₃	FW	1.37±0.20	0.959±0.20	52.7±11.2	0.69±0.24	1.29
	RW	1.36±0.19	0.956±0.11	54.5±7.9	0.72±0.19	1.04
CsPbBr ₃ :KI	FW	0.88±0.28	0.928±0.058	54.9±13.5	0.44±0.15	0.69
	RW	0.89±0.23	0.714±0.310	38.5±14.9	0.26±0.19	0.65

Table S4: Photovoltaic performance parameters of the CsPbBr₃ and CsPbBr₃:KI based devices (Day 20). The performance parameters are averaged over 12–18 devices. The ± sign shows the standard deviation of the performance parameters.

Active layer	FW/RW	J _{sc} (mA/cm ²)	V _{oc} (V)	FF (%)	PCE Avg (%)	PCE best (%)
CsPbBr ₃	FW	1.42±0.24	0.938±0.20	49.5±10.7	0.68±0.31	1.30
	RW	1.40±0.19	0.934±0.11	55.9±7.9	0.77±0.34	1.37
CsPbBr ₃ :KI	FW	0.93±0.27	0.935±0.022	59.9±13.4	0.50±0.13	0.69
	RW	0.91±0.23	0.790±0.251	41±14.9	0.30±0.19	0.64

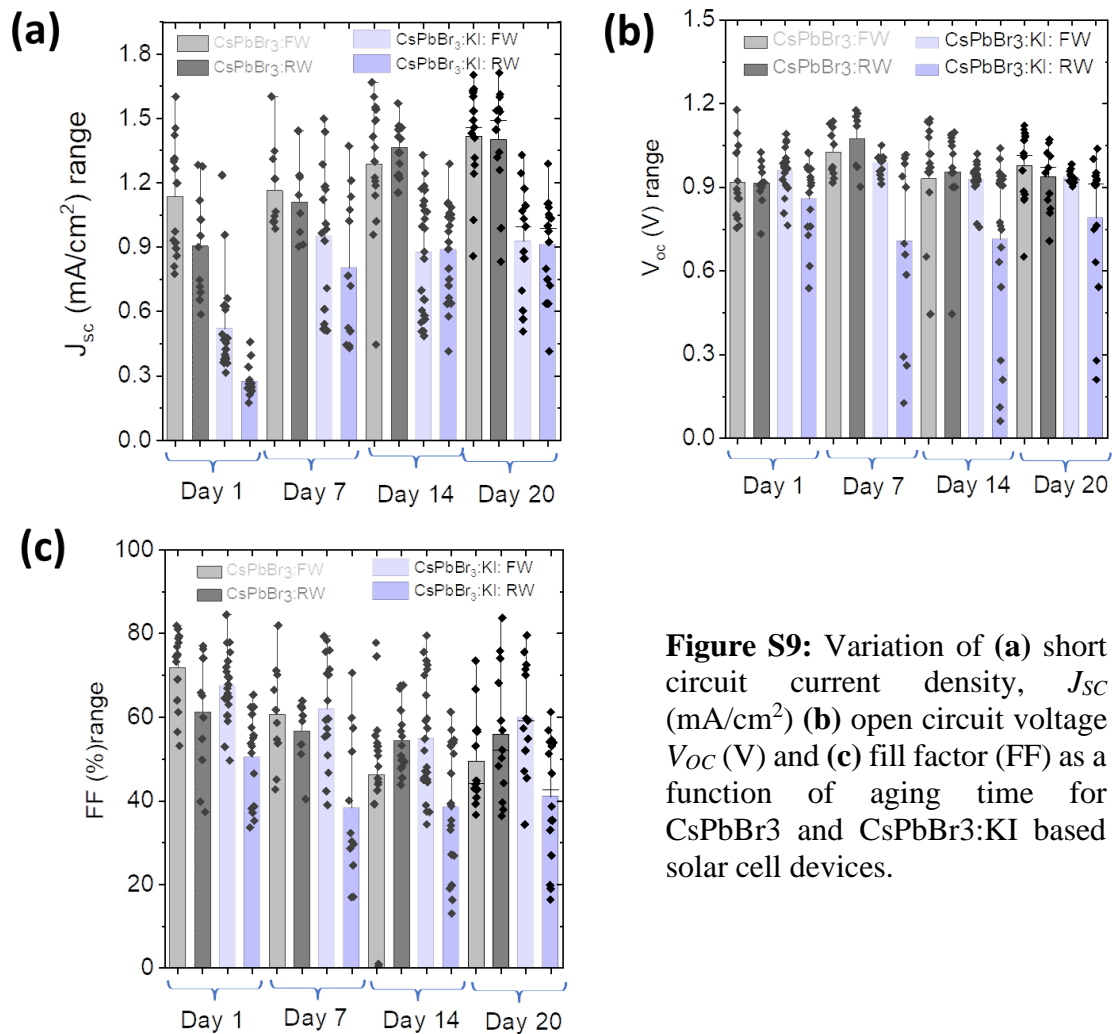


Figure S9: Variation of (a) short circuit current density, J_{sc} (mA/cm²) (b) open circuit voltage V_{oc} (V) and (c) fill factor (FF) as a function of aging time for CsPbBr₃ and CsPbBr₃:KI based solar cell devices.

Eliminating possible role of beam damage

Previous publications² and our own attempts to the CL mapping studies of hybrid-organic inorganic perovskites such as $\text{CH}_3\text{NH}_3\text{PbBr}_3$ had demonstrated the possible electron beam induced damage to the sample leading to the quenching of CL emission signal and change of spectral profile with time. CsPbBr_3 was selected for this study as the material is robust and with no organic component.³ For both CL spectroscopy and CL hyperspectral imaging, the electron beam current and voltage were selected such that CL signal was stable for the duration of mapping and no CL signal quenching was observed as a function of time.

CL signal stability was the primary condition set before proceeding to their mapping. For this CsPbBr_3 thin film samples prepared by two different methods were examined for CL emission and signal stability: (a) samples prepared by conventional route of mixing CsBr and PbBr_2 and (b) samples prepared using CsTFA (cesium trifluoroacetate) and PbBr_2 [as reported by Wang et al *Nat Comm.*2019, 10 665]. Though the CsPbBr_3 thin films prepared by the CsTFA route had brighter CL emission, the CL signal was quenching with time under electron beam scanning and hence was not used for further studies described in this manuscript. Though the exact reason is not known, it could be related to the beam damage of the organic trifluoroacetate anions, which was effectively passivating the surface defects. Thus, only CsPbBr_3 thin film samples prepared by mixing CsBr and PbBr_2 as described in the experimental method, were used for the present study as the CL signal was very stable for this sample set.

The exposure time was 50 ms for each pixel and the electron beam power was less than $5\mu\text{W}$ to prevent the degradation of the material. Three CL maps were collected for each sample to check the consistent and stable behavior of the CL signal. The secondary electron image of a CsPbBr_3 sample before and after the CL mapping is shown below. No noticeable beam damage was evident from these images. This resistance to beam damage was further supported by the observation of similar spectral shape and intensity of CL emission from the mapped region after completing the CL mapping.

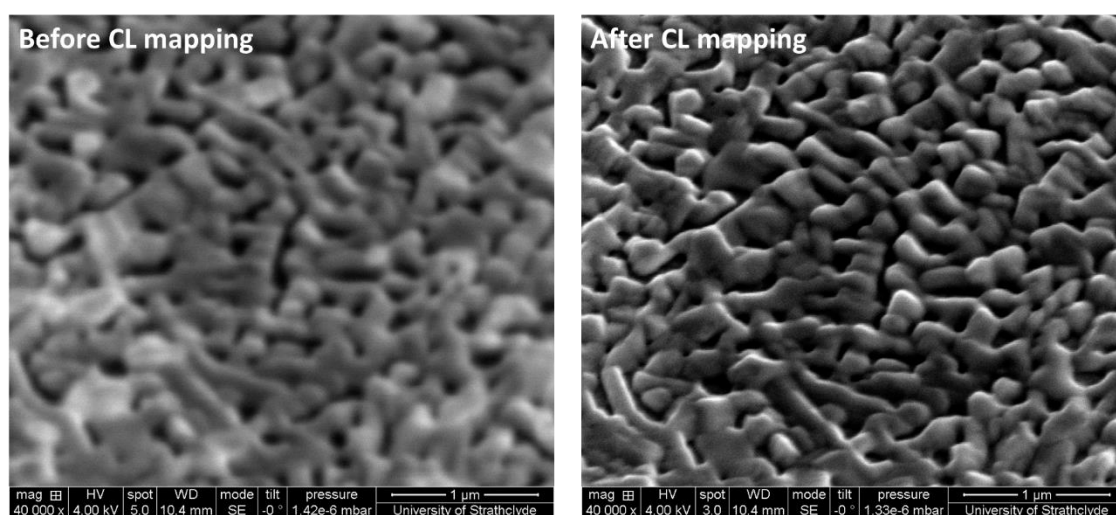


Figure S10: Secondary electron images of the CsPbBr_3 sample before and after CL hyperspectral mapping. A higher beam current was used for the CL measurements (in order to excite a sufficiently intense signal), while a lower current used to obtain SE images with high resolution. This high current (“spot 5” in terms specific to that SEM vendor) reduces the resolution of the images compared to the lower currents (“spot 3”).

Figure S11 below shows the comparison of the mean CL spectra from the three CL hyperspectral maps of CsPbBr₃:KI acquired at two different depths (50 nm and 130 nm) but approximately from the same region of the sample. The difference in intensity between the mean CL spectra from 50 nm and 130 nm depth is expected because the higher electron beam energy (4 kV vs 2 kV) applied to probe deeper regions of the sample would generate more electron-hole pairs. An intensity difference of 30-40 % is observed when approximately the same region is measured again and this is likely to be partly due to slight misalignment returning to nearly the same spot, inhomogeneity of the luminescence and partly due to a limited degree of beam damage. We attribute the lower energy CL tail to the presence of iodide rich mixed halide perovskites present in the mapped region.

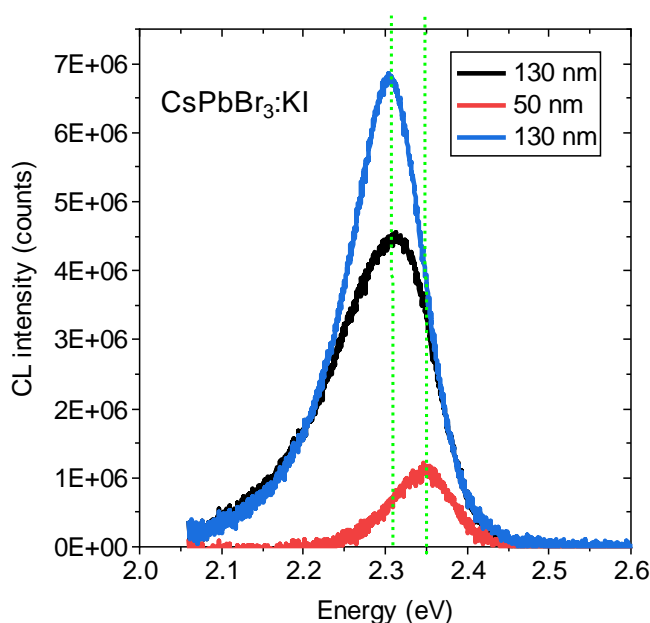


Figure S11: Mean CL spectra from three CL hyperspectral maps of CsPbBr₃:KI samples collected from two depths of 50 nm and 130 nm. The order of measurement is 130 nm, 50 nm and 130 nm again.

Obtaining 2D maps from the CL hyperspectral images

2D maps of intensity, peak energy and FWHM, such as those shown in Figure 2(c) –(f) and Figure 3 (main text), are obtained by applying multiple Gaussian peak fitting to each of 100 × 100 spectra in the CL hyperspectral image. This processing was carried out using a custom designed software tool (Cathodoluminescence Hyperspectral Imaging & Manipulation Program - CHIMP) developed by one of the corresponding authors (P.R.E.) of this manuscript. This uses Levenberg-Marquardt nonlinear least squares optimisation to achieve the fitting, yielding 2-dimensional maps of the resultant fit parameters (peak intensity, energy and FWHM). Suitable initial values and upper/lower limits are assigned to each parameter, which can also be fixed to avoid over-parameterisation of noisier data.

1. Tian, J.; Wang, J.; Xue, Q.; Niu, T.; Yan, L.; Zhu, Z.; Li, N.; Brabec, C. J.; Yip, H.-L.; Cao, Y. Composition Engineering of All - Inorganic Perovskite Film for Efficient and Operationally Stable Solar Cells *Advanced Functional Materials* **2020**, *30*, 2001764.
2. Klein-Kedem, N.; Cahen, D.; Hodes, G. Effects of Light and Electron Beam Irradiation on Halide Perovskites and Their Solar Cells *Accounts of Chemical Research* **2016**, *49*, 347-354.
3. Kulbak, M.; Gupta, S.; Kedem, N.; Levine, I.; Bendikov, T.; Hodes, G.; Cahen, D. Cesium Enhances Long-Term Stability of Lead Bromide Perovskite-Based Solar Cells *The Journal of Physical Chemistry Letters* **2016**, *7*, 167-172.